Lithos 376–377 (2020) 105764

Contents lists available at ScienceDirect

Lithos

journal homepage: www.elsevier.com/locate/lithos

Research Article

Origin of magmatic harzburgite as a result of boninite magma evolution – An illustration using layered harzburgite-dunite cumulate from the Troodos ophiolite complex

Fangyu Shen [a,b,c,d,*], Yaoling Niu [a,b,c,e,*], Yanhong Chen [b,e], Yajie Gao [f], Xiaohong Wang [a,c], Meng Duan [a,c], Li Shan [a,c,d]

[a] *Institute of Oceanology, Chinese Academy of Sciences, Qingdao 266071, China*
[b] *Department of Earth Sciences, Durham University, Durham DH1 3LE, UK*
[c] *Laboratory for Marine Geology, Qingdao National Laboratory for Marine Science and Technology, Qingdao 266061, China*
[d] *University of Chinese Academy of Sciences, Beijing 100049, China*
[e] *School of Earth Sciences and Resources, China University of Geosciences, Beijing 100083, China*
[f] *Research School of Earth Sciences, Australian National University, Canberra, ACT 2601, Australia*

ARTICLE INFO

Article history:
Received 30 March 2020
Received in revised form 1 September 2020
Accepted 4 September 2020
Available online 09 September 2020

Keywords:
Cumulate harzburgite
Petrogenesis
Boninite magma evolution
Troodos ophiolite
Fractional crystallization

ABSTRACT

Olivine (Ol) and orthopyroxene (Opx) are the primary liquidus phases of boninite in modern subduction settings and in many ophiolite complexes. It is thus straightforward to expect the formation of harzburgite cumulate resulting from boninite magma evolution. However, such magmatic harzburgite has been rarely studied. Here, we report the results of our study on such harzburgite from the Troodos ophiolite complex.

The Troodos cumulate harzburgite (locally lherzolite) is characteristically interlayered with dunite, showing varying thickness on millimeter to decimeter scales, as the result of volumetrically varying multiple pulses of melt injection into the evolving magma chamber. We illustrate the development of the interlayered cumulate by phase equilibrium analysis. The parental melt of each pulse begins to crystallize olivine to form a dunite layer before reaching the Ol-Opx cotectic, along which Ol and Opx coprecipitate to form a harzburgite layer. Periodical replenishment will result in dunite-harzburgite interlayered cumulate. In cases when replenishment may be delayed, the melt along the Ol-Opx cotectic can evolve to the Ol-Opx-clinopyroxene (Cpx) eutectic to form harzburgite with some Cpx or lherzolite. The calculated melts in equilibrium with spinels in the cumulate are characteristic of boninite in major element compositional spaces. The calculated melts in equilibrium with Cpx and Opx in the cumulate share the same as, or identical to, trace element patterns of the Troodos boninite (both glasses and bulk-rock compositions). Petrological modeling of the boninite magma evolution shows a crystallization order of Ol, Opx, Cpx, plagioclase. Our study also emphasizes the importance in considering dunite-harzburgite/lherzolite cumulate when interpreting seismic structure of the crust in subduction settings, especially in rock sequences associated with subduction initiation thought to be indicated by boninite magmatism.

© 2020 Elsevier B.V. All rights reserved.

1. Introduction

Harzburgite, dominated by olivine (Ol) and orthopyroxene (Opx), as mantle melting residue has been well understood (e.g., Dick et al., 1984; Jaques and Green, 1980; Niu, 1997, 2004), and as a cumulate constituent in layered intrusions has also been well studied (e.g., Cawthorn, 1996; Charlier et al., 2015). Because Ol and Opx are the primary liquidus phases of boninite in modern subduction settings and in many ophiolite complexes, it is expected that the boninite magma evolution will produce cumulate harzburgite. However, cumulate harzburgite as the result of boninite magma evolution has not been well documented and investigated. The cumulate harzburgite reported in layered intrusions was mostly ascribed to crystal settling or magma mixing in the magma chamber (e.g., Irvine and Smith, 1967; Raedeke and McCallam, 1984). On the basis of previous works and many years of our careful field observations, we have hypothesized that the ultramafic rock suites interlayered between dunite and harzburgite (locally lherzolite) in the Troodos Ophiolite complex must represent cumulate as the result of fractional crystallization of boninite magma evolutions. Indeed, boninite as dykes, veins and pillow lavas is widespread in the Troodos ophiolite complex (e.g. Cameron and Nisbet, 1979; Golowin et al., 2017; König et al.,

---

[*] Corresponding authors at: Institute of Oceanology, Chinese Academy of Sciences, Qingdao 266071, China.

E-mail addresses: fangyushen@qdio.ac.cn (F. Shen), yaoling.niu@durham.ac.uk (Y. Niu).

https://doi.org/10.1016/j.lithos.2020.105764
0024-4937/© 2020 Elsevier B.V. All rights reserved.

2008; Osozawa et al., 2012; Pearce and Robinson, 2010; Woelki et al., 2018). To test this hypothesis, we carried out detailed petrography, mineralogy, major and trace element geochemistry on both interlayered ultramafic suites and representative boninite samples from the Troodos ophiolite. These data, together with petrological modeling and phase equilibrium analysis, support the hypothesis that the interlayered dunite and harzburgite/lherzolite are straightforward consequences of boninite magma evolution in an open magma chamber system with periodic pulses of parental magma supply. The petrological significance is the new understanding on harzburgite petrogenesis. Our study complements previous studies and recognizes the interlayered ultramafic cumulates in the deep crustal section of the Troodos ophiolite complex as a consequence of boninite magma evolution. An important geodynamic implication is that care must be taken when interpreting seismic structure of the ocean crust in subduction settings, especially in rock sequences associated with subduction initiation where much of the boninite magmatism is thought to take place, which is of global significance.

In the following, we show our field and petrographic observations, discuss the data, and elaborate reasons that lead to our understanding and conclusions.

2. Geological setting

The Troodos ophiolite complex is one of the world's best preserved and studied ophiolites, which exposes in the central part of the island of Cyprus in the eastern Mediterranean. A complete ophiolite sequence comprising mantle peridotite, ultramafic to felsic plutonic complex, sheeted dykes, pillow lavas and pelagic sediments has been documented (Greenbaum, 1972; Moores and Vine, 1971). The Troodos ophiolite can be divided into the northern massif and the southern massif bounded by the Arakapas transform fault zone (Fig. 1). The age of the Troodos ophiolite is 90–92 Ma based on U-Pb dating of zircons from plagiogranite in the plutonic section (Konstantinou et al., 2007; Mukasa and Ludden, 1987), which has been confirmed recently using the advanced zircon U-Pb in situ dating method (Chen et al., 2020).

Although the Troodos ophiolite complex is well-studied, the tectonic setting in which it was formed remains in dispute. Previous studies suggest that the ophiolite could have formed in a juvenile arc, back-arc, fore-arc, slab-edge or ridge-trench-trench/transform triple junction setting (Osozawa et al., 2012; Pearce and Robinson, 2010; Regelous et al., 2014; Woelki et al., 2018). Fresh lavas have provided most useful information on the formation of the Troodos ophiolite. There have been varying divisions for the Troodos lavas based on their stratigraphy and geochemistry (e.g., Bednarz and Schmincke, 1994; Osozawa et al., 2012; Pearce and Robinson, 2010; Robinson et al., 1983; Smewing et al., 1975). The commonly accepted division includes three major suites: (1) a lower suite (lower pillow lava) of tholeiitic basalt, andesite, dacite to rhyolite, (2) a picritic, basaltic to andesitic upper pillow lava and (3) a boninitic suite cropping out mainly along the Arakapas Fault Zone (e.g., Flower and Levine, 1987; Thy and Xenophontos, 1991). We use this classification in our discussion for consistency. The boninite lava in Troodos is dated to be ~55 Ma based on the Ar-Ar age obtained by Osozawa et al. (2012), about 35 Myrs younger than the bulk Troodos ophiolite sequences of ~90 Ma (see above), indicating that they are unrelated.

The plutonic complex contains a series of ultramafic to gabbroic cumulate rocks overlying the mantle peridotite. The ultramafic cumulates exist in the lower levels of the plutonic complex, overlain by gabbros with or without cross-cutting basaltic dykes. Dunite, wehrlite, websterite and pyroxenite are most documented within the ultramafic cumulates (e.g., Batanova et al., 1996; Benn and Laurent, 1987; Greenbaum, 1972; Laurent, 1992; Thy, 1987a). The drill hole CY-4 (Fig. 1) sampled gabbros and ultramafic cumulates of coarse-grained websterites containing augite, enstatite, olivine and interstitial plagioclase (Thy, 1987a). Lowermost dunitic and wehrlitic cumulates were not sampled by the CY-4 drilling. The CY-4 data show that the contact between the lower cumulate complex and the upper gabbros is a petrographic and chemical discontinuity (Thy, 1987a, 1987b), probably in fault contact. In this study, we do not discuss the above cumulate, but focus on the uniquely interlayered dunite-harzburgite/lherzolite cumulate (Fig. 2a–c).

3. Samples and petrography

3.1. Field observations and samples

The Troodos ophiolite has an inverted stratigraphic sequence with mantle harzburgite on the top of the mountain (Mount Olympus),

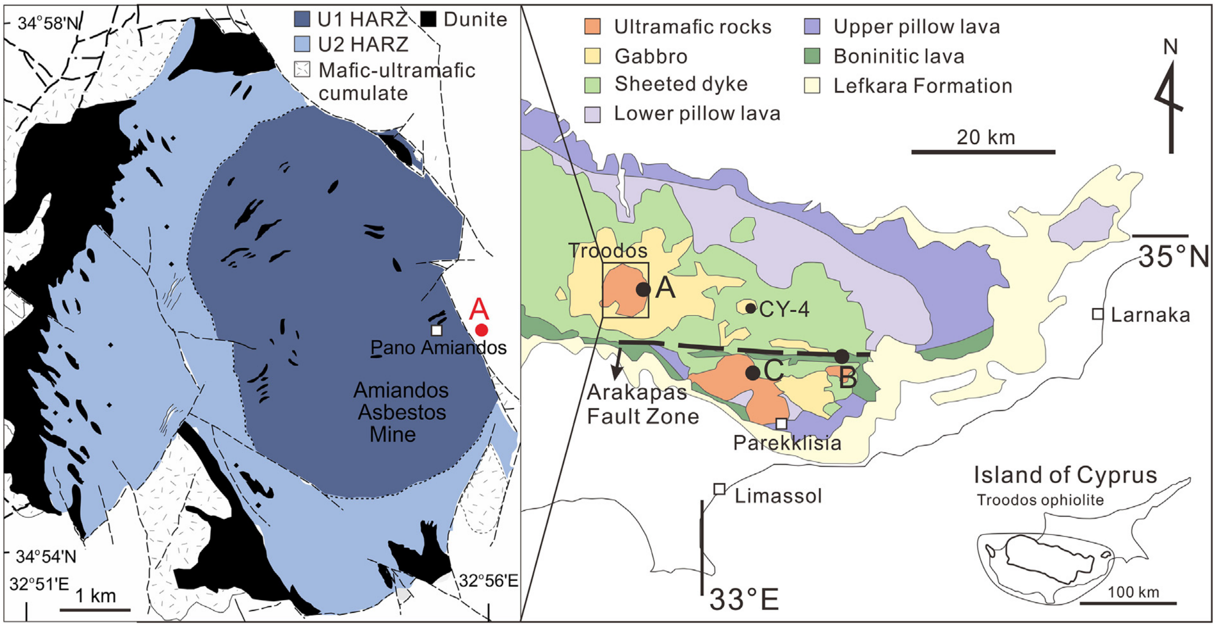

Fig. 1. Simplified geological map of the Troodos Ophiolite (modified from Batanova and Sobolev (2000) and Osozawa et al., 2012), showing sample locations (A–C). A: interlayered harzburgite/lherzolite and dunite; B: boninite as pillow lavas from the Arakapas Fault Zone (AFZ); C: boninite as dyke near the AFZ. CY-4 is a bore hole drilled into the lower sheeted dyke complex, gabbros and ultramafic cumulates (Thy et al., 1987a). U1 harzburgite and U2 harzburgite are mantle peridotites (Batanova and Sobolev, 2000).

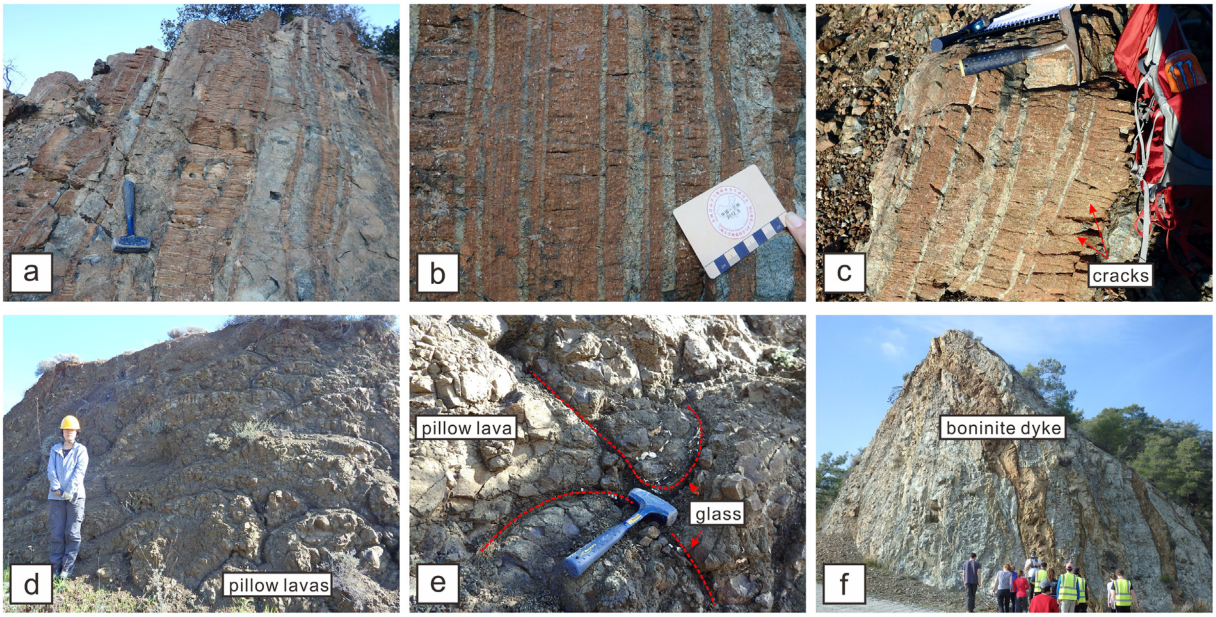

Fig. 2. Field photos of the interlayered ultramafic rocks near the Pano Amiandos and boninites from the Arakapas Fault Zone (AFZ) in the Troodos ophiolite complex. (a, b, c): Interlayered cumulate of serpentinized harzburgite (brown; or lherzolite if locally Cpx rich) and serpentinized dunite (dark grey) with varying thickness on decimeter (a) to millimeter (b) scales. Note that cracks perpendicular to the layering are confined within the harzburgite (a–c). (d, e): Piles of pillow lavas near the AFZ with fresh/altered glassy rinds well preserved. (f): Brownish subvertical boninite dykes cross-cutting basaltic dykes near the AFZ. (For interpretation of the references to colour in this figure legend, the reader is referred to the web version of this article.)

whereas the lower ultramafic cumulate, gabbros, sheeted dykes and lavas occur downhill in this order (Fig. 1). Therefore, cumulates and lavas are well separated. To test the aforementioned hypothesis on the possible genetic relationship between the interlayered ultramafic cumulate (dunite+harzburgite/lherzolite) and boninite, and to understand the petrogenesis of the ultramafic cumulate, we collected representative samples of the cumulate and boninite for a detailed petrological and geochemical study.

Field observations were documented in both northern massif and southern massif of the Troodos ophiolite complex. Our interpreted (hypothesized) ultramafic cumulate comprises serpentinized harzburgite/lherzolite (brown) interlayered with serpentinized dunite (dark grey) (Fig. 2a-c) outcropped on a NW-SE trending ridge, ~ 1 km east of Pano Amiandos, occurring as blocks in fault contact in the vicinity of the “petrologic Moho” between the massive mantle harzburgite (~ 300 m east of mantle harzburgite) and plutonic rocks on the east flank of Mount Olympus (A in Fig. 1, Table 1). These blocks are several meters wide and several meters to tens of meters high. The lithological layers vary in thickness from decimeters (Fig. 2a) to millimeters (Fig. 2b) with sharp and parallel contacts. The distinctive cracks perpendicular to the layering are confined in the harzburgite/lherzolite layers (absent in the adjacent dunite layers) (Fig. 2a–c), which is best understood as greater volume expansion of dunite (Ol) than harzburgite/lherzolite (Ol + Opx ± Clinopyroxene) during serpentinization (see Niu et al., 1997). We sampled the brown and the dark-grey layers of varying thickness.

Table 1
Location and mineral modes of the ultrmafic cumulate samples.

Sample	Latitude	Longitude	Lithology	Mineral modes (vol%)
TDS06–1	34°55′42″N	32°55′34″E	Dunite	Ol 97, Opx 3
			Lherzolite	Ol 51, Opx 32, Cpx 17
TDS06–2	34°55′42″N	32°55′34″E	Dunite	Ol 98, Opx 2
			Harzburgite	Ol 46, Opx 52, Cpx 2
TDS45–4	34°55′42.61″N	32°55′35.16″E	Dunite	Ol 98, Opx 2
			Harzburgite	Ol 49, Opx 46, Cpx 5
TDS45–5	34°55′42.61″N	32°55′35.16″E	Dunite	Ol 97, Opx 3
			Harzburgite	Ol 48, Opx 48, Cpx 4
TDS46	34°55′43.32″N	32°55′34.82″E	Dunite	Ol 94, Opx 6
			Lherzolite	Ol 41, Opx 35, Cpx 24
TDS47	34°55′44.53″N	32°55′34.07″E	Dunite	Ol 100

The minreal modes are determined by point-counting on 200–600 points in each kind of layers.

3.2. Petrography

Boninite samples near the Arakapas Fault Zone (AFZ) contain euhedral to subhedral phenocrysts of olivine, orthopyroxene and spinel (Fig. 3a). Olivine and pyroxene also occur as microlites in the glassy groundmass as the result of fast cooling and quench. The mineralogy and textures of these samples are very similar to the typical boninite from Hahajima Seamount, Bonin forearc (Li et al., 2013) and the modern boninite lava from the Lau Basin (Resing et al., 2011), and confirm the previous studies on the Troodos boninite (e.g., Cameron, 1985; Flower and Levine, 1987; Golowin et al., 2017; Robinson et al., 1983). The absence of plagioclase is a notable feature of typical boninite (e.g., Crawford et al., 1989; Resing et al., 2011; Robinson et al., 1983; Taylor et al., 1994).

Mineral modes of the ultramafic cumulate samples are done by point-counting (Table 1), indicating that the brown layers interlayered with dunite are dominated by harzburgite (locally lherzolite). The dunite layers are strongly serpentinized with only olivine cores left as relics. The dunite is characterized by typical mesh textures with olivine replaced by serpentine (Fig. 3b). In some dunite layers, the olivines are totally serpentinized (see the bottom two dunite layers in Fig. 4). The harzburgite layers are dominated by olivine and orthopyroxene without or with varying amount of clinopyroxene (Cpx), and have undergone varying degree of serpentinization. All the Ol, Opx and Cpx grains are cumulus phases. In most cases, Opx and Ol (~ 0.5–1 mm in size) are generally euhedral, showing textually equilibrated mosaic of equigranular grains as adcumulate (Fig. 3c, d). Some olivine grains also exhibit subhedral to anhedral shapes with irregular boundaries (see Fig. 3e, f). The Cpx often occurs as anhedral

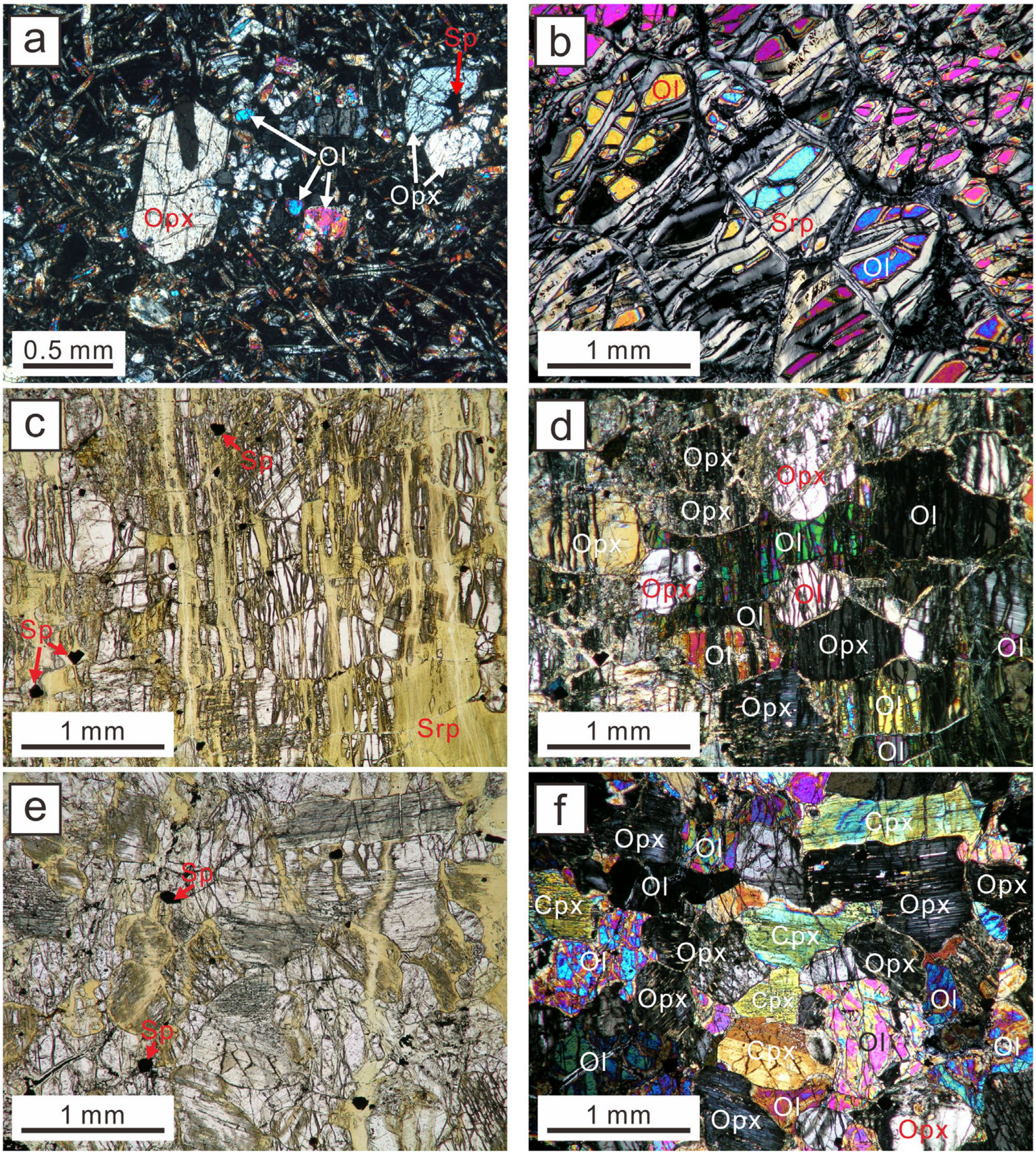

Fig. 3. Photomicrographs of boninite, dunite and harzburgite. (a): Boninite from the AFZ containing phenocrysts of euhedral and subhedral Ol, Opx and Sp, with Ol and pyroxene microlites in the glassy groundmass, very similar to typical boninite from Bonin forearc (Li et al., 2013) and the modern boninite lava from the Lau Basin (Resing et al., 2011). (b): Serpentinized dunite from the interlayered cumulate (dark grey layers in Fig. 2a–c). (c, d): Serpentinized harzburgite from the interlayered cumulate (brown layers in Fig. 2a–c). (e. f): Locally Cpx-rich lherzolite from a harzburgite layer of the interlayered cumulate (TDS06–1). Ol, Opx, Cpx, Sp and Srp are olivine, orthopyroxene, clinopyroxene, spinel and serpentine respectively. (a, b, d, f): crossed polarized light; (c, e): plane polarized light. (For interpretation of the references to colour in this figure legend, the reader is referred to the web version of this article.)

isolated grains (Fig. 3e, f). Interstitial Cpx also occurs poikilitically enclosing Opx locally. Some orthopyroxene grains have exsolution textures with clinopyroxene lamellae along cleavages (Fig. 3d, f). It is possible that these minute clinopyroxene grains may have developed into the “granular exsolutions” (see Niu, 2004), but most of the coarser-grained ones are clearly liquidus phase. Spinels are generally less than 0.2 mm in size and euhedral to anhedral in shape, often occurring along grain boundaries of Opx and Ol.

In order to show microscopic textures of the interlayered dunite and harzburgite/lherzolite cumulate as a whole, we piece together low magnification photomicrographs of a cumulate sample (TDS45–4) with relatively thin layers (2–15 mm) collected from the block shown in Fig. 2b (Fig. 4). The layers are well defined with clear contacts and transitions. The mineral modes given in Fig. 4 indicate that the harzburgite layers have varying Cpx and may be locally termed lherzolite if Cpx ≥ 10 vol% (not in this mosaic). The harzburgite shows typical cumulate texture though camouflaged by varying degrees of serpentinization with layer-perpendicular cracks filled with serpentines (see above and below). The dunite is strongly serpentinized, with few olivine relics in some of the layers. Spinels often appear as euhedral or subhedral crystals in the harzburgite layers, while fine-grained magnetite aggregates occur as bands in the interiors of the serpentine veins in dunite layers (Fig. 4 left). The layer-perpendicular cracks are filled with serpentines coming from the dunite layers. All the primary phases are subjected to serpentinization, but the rate and extent of serpentinization decrease in the order Ol, Opx and Cpx, with Ol-dominated dunite having volume expansion of up to ~30 wt%, significantly more than harzburgite (locally lherzolite) made up of Ol + Opx ± Cpx (Coleman and Keith, 1971; Niu et al., 1997; O'Hanley, 1992). As a result, the greater volume expansion of dunite layers causes layer-perpendicular cracks (filled with serpentines) in the adjacent harzburgite/lherzolite layers on both macroscopic (Fig. 2) and microscopic (Fig. 4) scales.

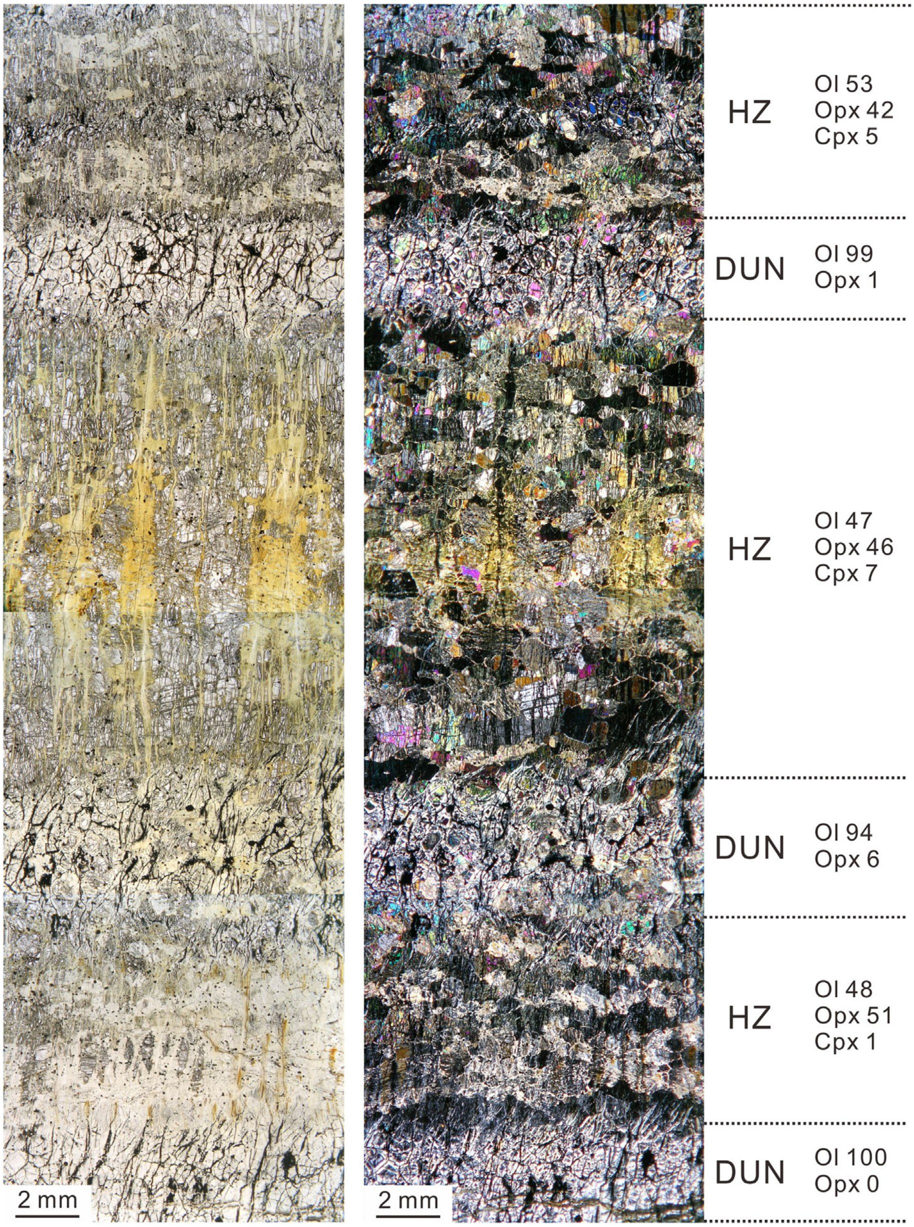

Fig. 4. Stitched photomicrographs (left, plane polarized light; right, crossed polarized light) of the interlayered ultramafic cumulate (TDS45–4). The lithology (HZ - harzburgite; DUN - dunite) and mineral (Ol - olivine; Opx - orthopyroxene; Cpx - clinopyroxene) modes (vol%) of each layer are indicated. These layers can be easily recognized with clear contacts. The harzburgite (HZ) is characterized by cumulate texture and has undergone varying degrees of serpentinization. The dunite is strongly serpentinized. Parallel fractures in the harzburgite (perpendicular to the layering) are filled with serpentines from the adjacent dunite layer, which are in accordance with macroscopic cracks (Fig. 2a-c), resulting from greater volume expansion of dunite during olivine serpentinization. Note the mineral modal heterogeneity on the petrographic scale.

4. Methods

4.1. Sample preparation

To study the petrographic details of the interlayered cumulate of dunite and harzburgite/lherzolite, we sampled the cumulate on millimeter scales (see Fig. 2b) for texture characterization and mineral analysis (TDS06 and TDS45). Two samples with layers of 2–5 cm thick (see Fig. 2c) were also collected for “bulk-rock” analysis (TDS46 and TDS47). The harzburgite interlayered with dunite in TDS46 is locally of high Cpx (vs. seen in Fig. 4) and is best termed lherzolite on the petrographic scale (see Table 1). In order to show the different chemical compositions between the brown and dark-grey layers, the two cumulate samples were cut carefully into 5 pieces of “pure” dunite and 4 pieces of “pure” harzburgite/lherzolite with surface contaminants thoroughly removed. Although the “bulk-rock” samples are variably serpentinized, the compositions of the cumulate dunite and harzburgite/lherzolite can be comparted on an anhydrous basis (see Niu, 2004) by normalizing major element compositions to 100%. These 9 sample fragments were then reduced to small (1–2 cm) chips and ultrasonically washed in Milli-Q water before dried and grinded into powder using agate mill in a clean environment for “bulk-rock” analysis.

Boninite samples from pillow lavas and dykes near the AFZ have phenocrysts and quenched microlites. To obtain melt compositions, 9 boninite samples were crushed into chips of 1–2 mm size, and only groundmass fractions free of phenocrysts were hand-picked under a binocular before ultrasonically cleaned in Milli-Q water. These chips were then embedded in epoxy and polished for laser-ablation inductively coupled plasma-mass spectrometer (LA-ICP-MS) analysis.

4.2. Analytical methods

Bulk-rock major element analysis of the interlayered ultramafic cumulate was done in the Laboratory of Ocean Lithosphere and Mantle Dynamics, Institute of Oceanology, Chinese Academy of Sciences (LOLMD-IOCAS) by using Agilent 5100 inductively coupled plasma-optical emission spectrometer (ICP-OES) following the method of Kong et al. (2019). The analytical precision is better than 5% (RSD, relative standard deviation). The values of USGS reference materials BCR-2, BHVO-2 and AGV-2 analyzed together with the samples agree well with the reference values within error.

For trace element analysis, 50 mg powder of each cumulate sample was dissolved with acid mix (1: 2) of distilled HF and aqua regia (1 HNO_3: 3 HCl) in a 15 mL Teflon beaker. The analysis was done using an Agilent 7900 inductively coupled plasma-mass spectrometer (ICP-MS) in the LOLMD-IOCAS following Chen et al. (2017). USGS reference rocks (BCR-2, BHVO-2, AGV-2, GSP-2 and W-2) analyzed as unknowns along with the samples give compositions the same as recommended values within error.

Major and trace elements of boninite samples and minerals (olivine, orthopyroxene, clinopyroxene and spinel) in the interlayered ultramafic cumulate samples were analyzed using a Photon Machines Excite 193 nm excimer Ar-F laser system attached to an Agilent 7900 ICP-MS in the LOLMD-IOCAS. Spot size used for analyzing glasses and lavas was 110 μm. For minerals, spot sizes were 85 μm for olivine, orthopyroxene and clinopyroxene and 25 μm for spinel. An energy density of 3.94 J/cm^2 at a repetition rate of 6 Hz were applied. Each analysis includes 25 s background acquisition

Table 2
Major and trace element analysis of boninite near the Arakapas Fault Zone.

Sample	TDS19A	TDS19C	TDS19D	TDS19E	TDS19F	TDS19G	TDS19H	TDS21	TDS87A
Location	AFZ	AFZ	AFZ	AFZ	AFZ	AFZ	AFZ	AFZ	AFZ
Type	Pillow	Pillow	Pillow	Pillow	Pillow	Pillow	Pillow	Dyke	Dyke
(wt%)									
SiO_2	55.45	55.58	53.25	55.81	52.57	55.75	53.59	51.67	56.81
TiO_2	0.246	0.166	0.275	0.265	0.236	0.27	0.287	0.42	0.206
Al_2O_3	16.66	16.74	15.51	16.66	15.48	14.92	14.44	15.25	17.79
FeOt	8.45	8.281	9.89	8.798	10.405	7.843	9.122	10.81	7.003
MnO	0.172	0.125	0.14	0.127	0.143	0.138	0.178	0.147	0.084
MgO	9.239	9.015	10.14	7.01	9.666	8.725	10.45	10.69	7.337
CaO	8.06	8.425	9.138	9.349	10.05	11.23	10.83	8.784	8.673
Na_2O	0.849	0.815	0.815	1.203	0.442	0.602	0.381	1.658	1.555
K_2O	0.426	0.31	0.37	0.331	0.506	0.108	0.249	0.1	0.157
P_2O_5	0.018	0.019	0.02	0.017	0.022	0.015	0.015	0.033	0.074
Total	99.56	99.48	99.54	99.56	99.46	99.63	99.54	99.56	99.69
Mg#	0.68	0.68	0.67	0.61	0.65	0.69	0.69	0.66	0.67
(ppm)									
Li	15.89	14.67	12.53	7.92	10.78	7.66	18.66	7.48	8.49
Sc	48.86	31.36	39.46	36.01	43.1	38.03	51.34	42.67	18.1
V	293.2	211.1	240.7	235.7	241.6	241.4	309.3	350.3	153.5
Cr	234.3	219.4	242.4	117.5	631.1	144.4	239.2	31	207.1
Co	40.7	47.14	42.39	33.3	44.64	36.14	47.55	51.28	30.25
Ni	117.1	995.3	194.2	99.18	240.6	122.4	193.3	147.5	133.9
Cu	218.1	213.6	191.3	201.5	159.8	196.3	208.5	36.65	21.15
Zn	99.42	159.12	113.71	78.96	101.04	64.93	96.39	109.8	72.06
Rb	7.758	5.65	6.861	4.991	8.327	2.086	5.165	0.575	0.954
Sr	231.1	135.6	110.7	437.3	148.9	300.2	161.9	47.67	51.67
Y	8.436	5.918	8.24	7.891	7.502	7.997	9.256	9.202	8.163
Zr	5.695	4.182	6.034	6.436	4.583	6.184	6.212	18.07	7.398
Nb	0.588	0.394	0.85	0.856	0.437	0.705	0.806	1.627	0.857
Sn	0.664	0.791	0.735	0.385	0.453	0.28	0.316	0.516	0.335
Cs	0.447	0.249	0.338	0.494	0.359	0.126	0.271	0.018	0.02
Ba	20.47	34.47	39.44	34.63	50.32	54.46	28.59	7.32	9.489
La	0.383	0.292	0.479	0.39	0.257	0.429	0.366	0.64	1.374
Ce	0.684	0.559	0.856	0.826	0.559	0.829	0.806	1.432	2.606
Pr	0.104	0.075	0.117	0.105	0.077	0.111	0.116	0.194	0.297
Nd	0.574	0.374	0.603	0.55	0.399	0.552	0.586	0.871	1.401
Sm	0.271	0.207	0.286	0.302	0.209	0.293	0.342	0.418	0.493
Eu	0.116	0.086	0.132	0.117	0.099	0.147	0.144	0.172	0.191
Gd	0.625	0.426	0.625	0.628	0.503	0.665	0.724	0.811	0.813
Tb	0.126	0.092	0.14	0.129	0.103	0.142	0.158	0.18	0.138
Dy	1.11	0.81	1.132	1.107	0.943	1.151	1.28	1.45	1.216
Ho	0.289	0.201	0.296	0.267	0.238	0.288	0.322	0.351	0.252
Er	0.961	0.713	0.98	0.963	0.787	0.971	1.091	1.121	0.857
Tm	0.159	0.113	0.149	0.147	0.124	0.153	0.169	0.17	0.099
Yb	1.133	0.926	1.082	1.136	0.952	1.175	1.27	1.296	0.845
Lu	0.191	0.138	0.184	0.177	0.154	0.182	0.213	0.203	0.103
Hf	0.225	0.161	0.224	0.235	0.184	0.245	0.253	0.592	0.224
Ta	0.038	0.028	0.051	0.056	0.032	0.052	0.053	0.126	0.049
W	0.256	0.167	0.191	0.358	0.182	0.237	0.268	0.284	0.118
Pb	4.922	4.805	3.994	4.225	3.194	2.066	1.945	3.523	3.772
Th	0.115	0.101	0.108	0.125	0.089	0.13	0.111	0.253	0.15
U	0.091	0.061	0.095	0.1	0.057	0.096	0.106	0.183	0.116

AFZ, Arakapas Fault Zone; FeOt, total Fe; Mg# = Mg/(Mg + Fe^{2+}) (note: 10% total Fe is assumed to be Fe^{3+} in the calculation). Data of each sample have been averaged over 5 spots.

(gas blank) followed by 50 s data acquisition. USGS glasses (BCR-2G, BHVO-2G and BIR-1G) were used as multiple reference materials for external calibration following Liu et al. (2008). In combination with the summed metal oxide normalization method and time-drift correction according to the variations of NIST 610, the matrix effect and instrumental drift can be effectively corrected (Liu et al., 2008). The raw data were processed using ICPMSDataCal_ver11.0 (Liu et al., 2008). Data quality was assessed by the result of USGS reference materials and the repeated analyses of GSE-1G over the analytical session (Supplementary Table S1, S2). For major elements with concentrations >0.1 wt%, the accuracies (relative error between measured and recommended values) and precisions (RSD) for USGS glasses are generally better than 5%. The reproducibility of GSE-1G is better than 5% for most of the major element analyses of glass, olivine, pyroxene and spinel, except for TiO_2, Cr_2O_3, MnO, NiO, ZnO and V_2O_5 (RSD < 10%) in spinel analysis, which is due to the small ablation spot size (25 μm). For most trace elements, the accuracy and precision of USGS glasses and GSE-1G are better than 5% (Supplementary Table S3). The analytical details are given in Xiao et al. (2020).

5. Results

5.1. Major and trace element compositions of the boninite

There are recent analyses on fresh boninite glasses from the Troodos ophiolite available (Golowin et al., 2017; König et al., 2008; Woelki et al., 2018). Here we present some new data on major and trace elements of boninite pillow lavas and dykes from the AFZ (Table 2).

The major element compositions of the samples near the AFZ are consistent with typical boninite (MgO > 8 wt%, TiO_2 < 0.5 wt% and SiO_2 > 52 wt%; Le Bas, 2000). The slightly more evolved samples with lower MgO (7.0–7.3 wt%) are similar to the compositions of some boninite glass samples (Golowin et al., 2017; Woelki et al., 2018). The Troodos boninite is classed as high-Ca boninite because of the high CaO/Al_2O_3 value (always >0.75; Crawford et al., 1989), while boninite samples in this study have CaO/Al_2O_3 of 0.48–0.75. The trace element compositions of the boninite near the AFZ overlap well with the literature data on boninite glasses (Golowin et al., 2017; Woelki et al., 2018; Fig. 5). The REE patterns of the boninite samples show obvious "U shape" (Fig. 5a), and there is notable enrichment in fluid soluble

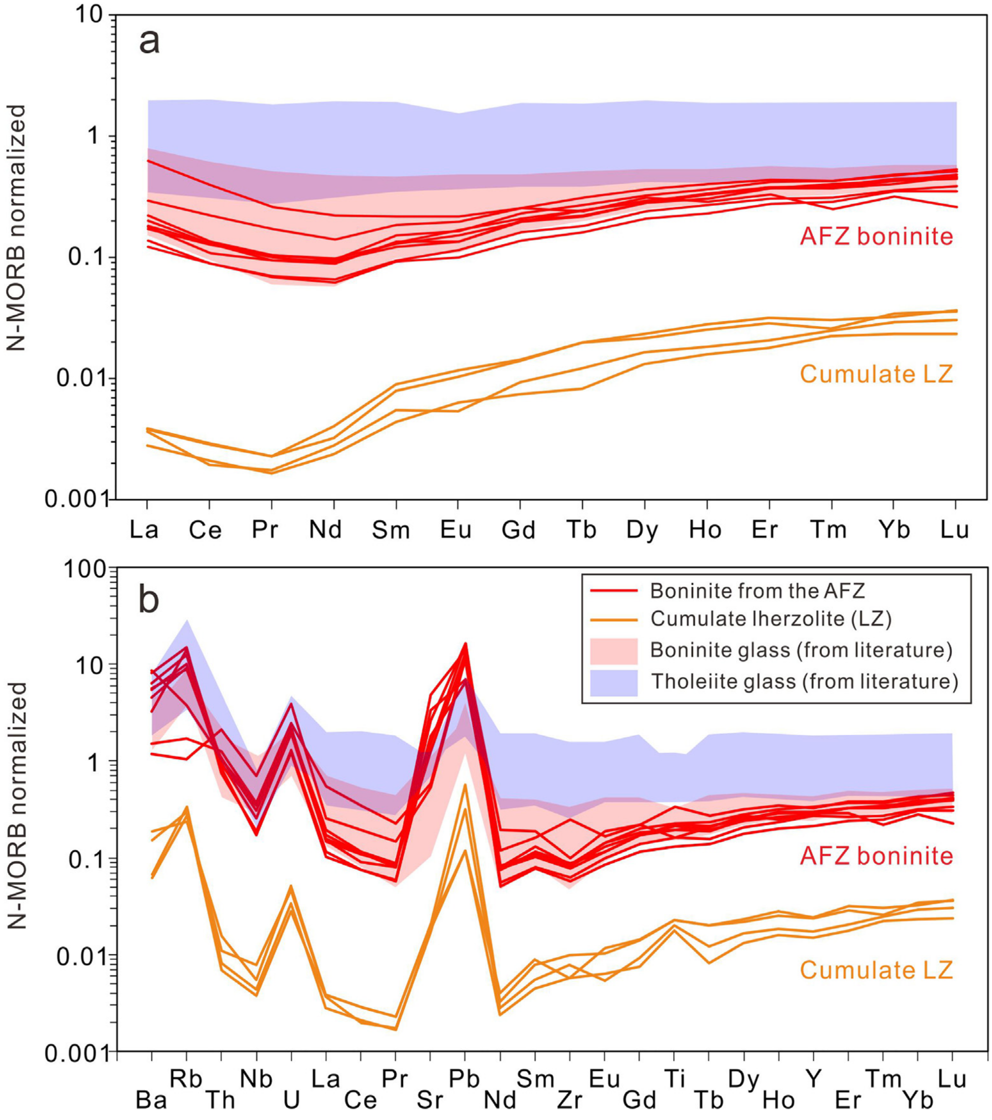

Fig. 5. N-type MORB (Sun and McDonough, 1989) normalized REE (a) and multielement (b) patterns of the boninite from the Arakapas Fault Zone (AFZ) and the bulk-rock cumulate lherzolite (locally Cpx rich from the harzburgite layer). Fields of boninite glass (Golowin et al., 2017; Woelki et al., 2018) and tholeiite glass from the Akaki Canyon (Regelous et al., 2014) are shown for comparison. There is notable enrichment in fluid soluble elements (e.g., Ba, Rb, U, Sr and Pb) in both samples of boninite near the AFZ and the cumulate lherzolite relative to N-MORB. The boninite near the AFZ has a characteristic U-shape REE pattern, which can be distinguished from the tholeiite glass in Troodos.

elements (e.g., Ba, Rb, U, Sr and Pb) in boninite samples characteristic of subduction-related magmas (Fig. 5b). The U-shaped REE pattern is characteristic of boninite magmas as a result of addition of light rare earth element (LREE) enriched component to a refractory peridotite mantle source (Cameron et al., 1983; Crawford et al., 1989). All these observations confirm that the boninite samples near the AFZ are typical boninite.

5.2. Bulk-rock major and trace elements of the interlayered ultramafic cumulate

Bulk-rock major and trace element compositions of 5 dunite and 4 lherzolite (locally Cpx rich from the harzburgite layer; see above) cumulate samples are given in Table 3. The major element compositions are normalized to 100% on an anhydrous basis because of serpentinization related loss on ignition (LOI: 6.0–12.8 wt% for dunite and < 1.6 wt% for lherzolite from locally Cpx rich harzburgite layer). The data show obvious differences between the dark grey (dunite) and brown (harzburgite/lherzolite) layers as expected on the basis of field and petrographic observations. The dark grey layers have lower average SiO_2 (44.42 wt%), Al_2O_3 (0.43 wt%), CaO (0.27 wt%), but higher FeOt (11.84 wt%) and MgO (44.61 wt%), whereas the brown layers have higher average SiO_2 (52.52 wt%), Al_2O_3 (1.7 wt%), CaO (5.75 wt%), but lower FeOt (7.99 wt%) and MgO (31.76 wt%). In terms of bulk-rock incompatible trace element compositions, the lherzolite from locally Cpx rich harzburgite layer has similar characteristics (U-shaped REE pattern and enrichment in fluid soluble elements, see above) but lower concentration levels than the Troodos boninite (Fig. 5), which indicates a possible genetic link between the two.

Table 3
Bulk-rock major and trace elements of the interlayered ultrmafic cumulate.

Sample	TDS46–1	TDS46–3	TDS46–5	TDS46–7	TDS46–2	TDS46–4	TDS46–8	TDS47–1	TDS47–2
LITH	HZ/LZ	HZ/LZ	HZ/LZ	HZ/LZ	DUN	DUN	DUN	DUN	DUN
(wt%)									
SiO_2	52.72	53.34	52.56	51.45	43.17	44.26	45.49	40.2	40.22
TiO_2	0.03	0.026	0.033	0.027	0.004	0.011	0.011	0.004	0.004
Al_2O_3	1.795	1.669	1.809	1.521	0.304	0.678	0.659	0.259	0.264
FeOt	7.658	8.058	7.551	8.685	13.59	12.63	11.83	10.59	10.57
MnO	0.189	0.201	0.193	0.186	0.085	0.107	0.141	0.155	0.156
MgO	30.64	31.81	30.47	34.1	42.79	41.65	41.31	48.64	48.65
CaO	6.903	4.831	7.32	3.942	0.04	0.615	0.494	0.086	0.103
Na_2O	0.053	0.048	0.053	0.06	0.006	0.021	0.023	0.012	0.015
K_2O	–	–	–	–	–	–	–	–	–
P_2O_5	0.009	0.013	0.009	0.033	0.015	0.025	0.039	0.057	0.016
Total	100	100	100	100	100	100	100	100	100
Mg#	0.88	0.88	0.88	0.87	0.85	0.85	0.86	0.89	0.89
(ppm)									
Li	1.345	1.514	1.31	1.309	0.409	0.505	0.414	0.039	0.038
Sc	31.76	27.82	31.5	24.28	4.335	8.208	10.4	4.677	4.579
V	102.5	91.62	102.6	85.77	16.28	35.66	37.67	19.12	23.02
Cr	4837	4835	4696	5359	2291	3857	3182	3543	4334
Co	62.22	63.98	60.69	75.39	129.3	112.7	113.5	113.3	115.5
Ni	488.4	484.6	474.4	625.1	1208	1082	1117	1453	1463
Cu	4.462	3.21	3.586	3.493	1.484	1.205	1.28	1.451	1.407
Zn	38.56	38.67	37.76	42.24	32.12	39.03	46.63	41.74	52.89
Ga	1.445	1.384	1.416	1.321	0.415	0.712	0.67	0.47	0.562
Rb	0.152	0.165	0.133	0.188	0.023	0.038	0.091	0.044	0.053
Sr	1.8	1.526	1.846	1.617	0.309	0.784	1.51	0.312	0.731
Y	0.667	0.481	0.677	0.421	0.028	0.156	0.122	0.036	0.06
Zr	0.733	0.58	0.425	0.422	0.168	0.226	0.196	0.143	0.196
(ppb)									
Nb	18.2	8.72	12.71	10.19	13.41	11.51	9.486	9.801	9.398
Mo	69.46	18	24.18	345.3	32.06	26.79	26.27	30.46	27.34
Cs	2067	2516	1650	2570	34.43	246.3	393.9	175.5	152.2
Ba	392	969.3	1171	426.7	109.4	1142	2199	81.76	62.03
La	9.587	9.17	9.664	7.033	2.512	28.24	12.12	2.289	4.333
Ce	21.55	14.71	21.76	15.75	6.846	61.25	17.79	5.234	7.347
Pr	3.04	2.3	3.031	2.184	0.191	6.835	1.996	0.065	0.298
Nd	23.86	20.54	29.38	17.45	3.427	29.16	12.72	5.73	7.741
Sm	20.83	14.37	23.44	11.66	1.248	10.6	2.388	2.927	2.996
Eu	10.54	5.459	11.87	6.49	0.821	3.654	2.738	0.453	0.929
Gd	51.64	34.42	52.53	27.62	1.591	14.59	6.388	1.922	3.477
Tb	13.37	8.124	13.35	5.532	0.001	2.534	1.049	0.119	0.118
Dy	98.59	75.64	106.1	60.18	2.537	23.37	16.02	3.763	7.06
Ho	25.5	18.68	28.08	16.13	0.567	6.302	3.958	0.769	1.402
Er	84.38	61.46	94.9	52.78	1.631	22.21	17.1	3.504	4.946
Tm	11.84	11.26	13.87	10.15	0.001	3.208	2.656	0.444	0.712
Yb	104.46	89.98	97.96	71.24	6.91	29.39	28.75	7.334	9.007
Lu	16.24	13.78	16.77	10.72	1.323	4.336	4.918	0.859	1.368
Hf	20.34	16.76	14.9	14.06	4.052	7.486	5.954	2.456	3.278
Ta	22.42	14.52	12.82	11.57	20.12	14.73	11.06	14.67	14.58
Pb	168.8	94.12	35.33	35.72	36.42	153	72.36	26.93	115.4
Th	1.326	0.833	1.88	0.981	0.527	2.131	1.252	0.517	0.365
U	2.156	1.33	2.422	1.574	2.587	3.404	1.326	1.055	0.73

LITH, lithology; HZ/LZ, harzburgite/lherzolite; DUN, dunite; FeOt, total Fe; Mg# = $Mg/(Mg + Fe^{2+})$ (total Fe is assumed to be Fe^{2+} in dunite and harzburgite/lherzolite).

5.3. Mineral chemistry

The average major element compositions of olivine, spinel, orthopyroxene and clinopyroxene and trace element compositions of orthopyroxene and clinopyroxene in different samples are given in Table 4 and Table 5 with individual analyses given in Supplementary Table S4 – S7.

The forsterite content for olivine (Fo) from the cumulate dunite varies from 87 to 89. The olivine phenocrysts in boninite glasses from the literature (Golowin et al., 2017) are more Mg-rich (the mean Fo is 89) with a larger Fo range (85–91) (Fig. 6). This indicates that the melt in equilibrium with olivine from the cumulate dunite is more evolved than the erupted boninite melt. This is expected in an evolving magma chamber with multiple pulses of melt injection (see below). We didn't have the composition of olivine in the harzburgite/lherzolite layer because of pervasive of serpentinization with very rare relicts for analysis.

Orthopyroxene and clinopyroxene are both observed in the cumulate harzburgite/lherzolite. We analyzed 55 Opx grains and 33 Cpx grains from the harzburgite/lherzolite layers (Table 5). The Mg# varies from 0.88 to 0.89 and 0.89 to 0.91 in Opx and Cpx respectively. Orthopyroxene has lower CaO (0.97–3.99 wt%), TiO_2 (0.02–0.03 wt%), Cr_2O_3 (0.42–0.63 wt%), slightly lower Al_2O_3 (1.25–1.64 wt%) and higher MgO (31.73–33.52 wt%), FeOt (7.00–7.84 wt%), SiO_2 (53.71–56.49 wt%) than clinopyroxene. The major element compositions of Cpx in the cumulate harzburgite/lherzolite differ greatly from those in mantle harzburgite of the Troodos ophiolite (Batanova and Sobolev, 2000) with lower Mg#, CaO, Al_2O_3, Cr_2O_3 and higher FeOt (Fig. 7). The ultramafic cumulates collected by Coogan et al. (2003) show large Cpx major element compositional variations, but the Cpx in the ultramafic cumulates near the Amiandos we study shows quite uniform composition (Fig. 7). For trace element compositions, Opx has N-MORB normalized incompatible element patterns similar to those of Cpx and boninite, but has lower concentrations (see below).

Table 4
Major element compositions of olivine in the dunite and spinel in harzburgite/lherzolite and dunite.

Sample	Olivine				Spinel		
	TDS06–1	TDS06–2	TDS45–4	TDS45–5	TDS45–4	TDS06–2	TDS47–1
N	22	10	15	10	6	8	6
SiO_2	40.19	40.47	39.76	40.76	0.069	1.596	0.551
TiO_2	<0.01	<0.01	<0.01	<0.01	0.139	0.136	0.141
Al_2O_3	<0.01	<0.01	<0.01	<0.01	19.51	18.48	18.19
Cr_2O_3	<0.01	<0.01	<0.01	<0.01	43.76	42.18	42.3
FeOt	11.67	11.51	11.54	12.22	25.39	25.85	25.61
MnO	0.183	0.185	0.182	0.191	0.276	0.295	0.299
MgO	47.34	47.23	47.92	46.21	9.476	9.908	11.43
CaO	0.054	0.053	0.053	0.049	0.021	0.108	0.159
NiO	0.182	0.183	0.182	0.186	0.056	0.081	0.078
ZnO	<0.01	<0.01	<0.01	<0.01	0.235	0.287	0.247
V_2O_5	<0.01	<0.01	<0.01	<0.01	0.287	0.267	0.252
Total	99.62	99.63	99.63	99.61	99.21	99.13	99.18
Fo	87.85	87.98	88.1	87.08	–	–	–
Mg#	–	–	–	–	0.456	0.454	0.538
Cr#	–	–	–	–	0.601	0.605	0.61
Fe^{3+}#	–	–	–	–	0.071	0.066	0.11
Fe^{2+}/Fe^{3+}	–	–	–	–	3.864	4.932	2.395
Fe^{3+}/Fet	–	–	–	–	0.206	0.181	0.312

Major element oxides are in wt%. N, numbers for mineral crystals averaged in each sample. Note that each sample contains several layers. Fo = $Mg/(Mg + Fe^{2+}) \times 100\%$ (total Fe is assumed to be Fe^{2+} in olivine).
The spinel analyses are recalculated on the basis of 32 oxygen atoms per formula unit. Fe^{2+} and Fe^{3+} in spinel were calculated from stoichiometry (Droop, 1987) and Mg# = $Mg/(Mg + Fe^{2+})$, Fe^{3+}# = $Fe^{3+}/(Cr + Al + Fe^{3+})$ and Fet (total Fe) = $Fe^{2+}+Fe^{3+}$.

Table 5
Major and trace element compositions of orthopyroxene and clinopyroxene in cumulate harzburgite/lherzolite.

Sample	Orthopyroxene				Clinopyroxene	
	TDS06–1	TDS06–2	TDS45–4	TDS45–5	TDS06–1	TDS45–5
N	26	14	10	5	30	3
SiO_2	55.68	55.26	55.56	56.13	52.29	53.08
TiO_2	0.027	0.026	0.025	0.028	0.051	0.046
Al_2O_3	1.445	1.380	1.390	1.455	2.138	1.923
Cr_2O_3	0.557	0.539	0.533	0.567	0.898	0.869
FeOt	7.231	7.555	7.524	7.550	3.644	3.954
MnO	0.186	0.202	0.192	0.195	0.130	0.162
MgO	32.61	32.81	32.78	31.94	19.15	19.02
CaO	1.960	1.917	1.687	1.832	21.437	20.668
Na_2O	0.007	0.012	0.011	0.008	0.080	0.080
K_2O	0.0002	0.0005	0.0003	0.0003	0.0006	0.0014
Total	99.71	99.70	99.70	99.71	99.82	99.81
Mg#	0.89	0.89	0.89	0.88	0.90	0.90
(ppm)						
P	14.73	16.76	12.19	10.43	11.22	12.10
Sc	29.12	28.64	28.11	29.74	59.90	52.04
V	84.64	79.60	78.32	86.13	181.0	167.5
Co	68.07	61.63	62.18	62.98	32.24	31.97
Ni	409.3	373.0	389.8	367.5	239.9	232.9
Cu	0.398	0.507	1.365	0.459	0.753	1.749
Zn	39.98	40.51	42.11	42.68	13.90	17.62
Ga	1.499	1.338	1.445	1.570	1.964	1.906
Ge	1.813	1.748	1.917	2.153	1.959	1.971
Rb	0.043	0.037	0.040	0.075	0.042	0.186
Sr	0.074	0.166	0.143	0.170	2.156	2.341
Y	0.311	0.293	0.278	0.293	1.765	1.446
Zr	0.036	0.051	0.042	0.050	0.220	0.193
(ppb)						
Nb	2.502	4.383	3.053	4.565	7.761	12.95
Cs	176.5	616.0	127.5	427.5	151.2	1640
Ba	21.23	20.74	109.8	21.91	85.83	268.9
La	1.057	1.238	0.899	1.491	8.248	9.857
Ce	1.556	1.639	1.409	2.075	33.00	33.53
Pr	0.839	0.611	1.161	0.829	8.082	7.492
Nd	6.242	6.860	3.640	4.022	77.89	70.49
Sm	5.993	4.804	4.472	2.881	63.38	49.82
Eu	1.720	1.579	2.033	1.750	34.89	30.57
Gd	11.69	8.977	12.29	12.21	162.2	141.7
Tb	3.813	2.561	2.961	3.752	37.28	31.03
Dy	39.72	36.35	32.69	33.06	295.2	249.2
Ho	12.33	9.208	9.393	9.541	69.07	53.33
Er	46.04	36.06	41.22	44.33	214.5	181.3
Tm	8.970	6.523	7.842	7.962	31.72	26.24
Yb	72.37	61.31	62.52	68.76	209.6	175.4
Lu	12.77	9.50	10.38	12.62	29.68	25.29
Hf	3.104	3.453	3.379	2.883	17.16	13.00
Ta	0.479	0.644	0.206	0.475	0.470	0.609
Pb	195.2	57.98	185.0	112.3	114.1	53.12
Th	0.514	0.299	0.459	0.308	0.825	1.194
U	0.320	0.429	0.327	0.348	0.826	1.176

Major element oxides are in wt%. N, numbers for mineral crystals averaged in each sample. Note that each sample contains several layers. Mg# = $Mg/(Mg + Fe^{2+})$ (total Fe is assumed to be Fe^{2+} in Opx and Cpx).

Twenty spinel crystals from the cumulate harzburgite and dunite were analyzed with varying Cr_2O_3 (39.24–45.56 wt%), Al_2O_3 (15.56–21.01 wt%) and TiO_2 (0.11–0.18 wt%). In the trivalent Cr-Al-Fe^{3+} ternary cation diagram (Fig. 8a), the spinels in the ultramafic cumulate fall within the ophiolite chromite compositional field between the fields of boninite and abyssal peridotite spinels, which can be classified as Al-chromite (Stevens, 1944). Compared with the compositions of spinel in boninite glass of the Troodos ophiolite (Golowin et al., 2017; Woelki et al., 2018), spinels in the ultramafic cumulate have lower Cr# (Cr# = Cr/(Cr + Al) = 0.56–0.64 with an average of 0.61) and slightly higher Mg# (Mg# = $Mg/(Mg + Fe^{2+})$ = 0.39–0.57 with an average of 0.48), which is similar to forearc peridotite (Fig. 8b), suggesting a subducting-zone setting.

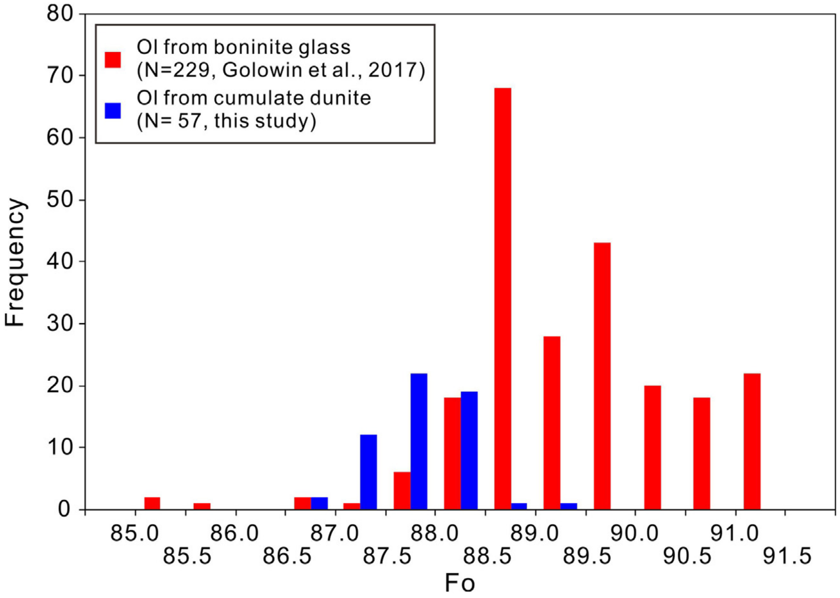

Fig. 6. Histogram of forsterite content for olivine (Fo) from the boninite and the cumulate dunite in the Troodos ophiolite. Olivine from boninite (Golowin et al., 2017) has more variable and higher Fo values than those from the cumulate dunite, indicating that the erupted boninite is more primitive than melt in equilibrium with olivine from the cumulate, which is actually expected (see text). Fo = 100 × Mg/(Mg + Fe^{2+}) (total Fe is assumed to be Fe^{2+} in olivine).

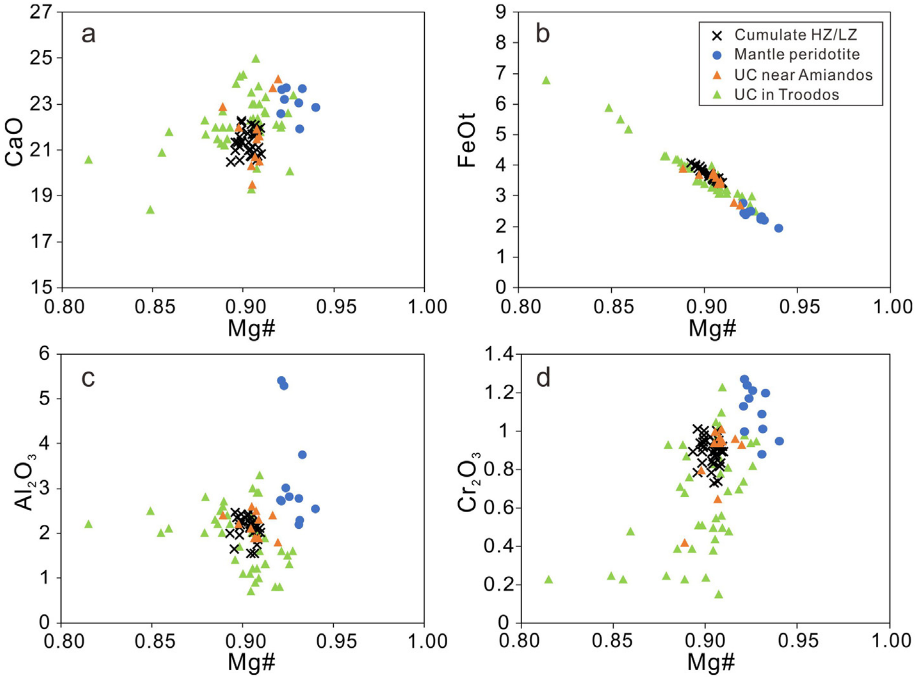

Fig. 7. Mg#-variation diagrams of CaO, FeOt, Al_2O_3 and Cr_2O_3 for clinopyroxene from the cumulate harzburgite (HZ)/lherzolite (LZ). Compositions of clinopyroxene from the Troodos mantle peridotite (Batanova and Sobolev, 2000) and the Troodos ultramafic cumulate (UC) near Amiandos (Coogan et al., 2003) are shown for comparison. There are notable differences between Cpx in the mantle peridotite and Cpx in the cumulate HZ/LZ. Cpx from the UC near Amiandos share similar compositions with Cpx from the cumulate HZ/LZ.

6. Discussion

6.1. Petrographic evidence for genetic link of boninite with the layered ultramafic cumulate

As shown above, boninite samples near the AFZ contains phenocrysts of olivine, orthopyroxene and spinel with olivine and pyroxene microlites without plagioclase (Fig. 3a), characteristic of typical boninite (e.g., Crawford et al., 1989; Li et al., 2013; Resing et al., 2011; Taylor et al., 1994). Experimental studies on the petrogenesis of boninite indeed indicate that olivine and orthopyroxene are primary liquidus phases followed by clinopyroxene with plagioclase (Plg) appearing very late on the liquidus (Duncan and Green, 1987; Falloon and Danyushevsky, 2000). Studies on boninite from the AFZ further show a crystallization order of chromite, olivine, orthopyroxene, clinopyroxene and plagioclase, which differs from basalt, basaltic andesite and andesite glasses from the upper pillow lava that are consistent with a crystallization order of chromite, olivine, clinopyroxene and plagioclase (Flower and Levine, 1987; Thy and Xenophontos, 1991). We can thus reason that the dunite (Ol) and harzburgite/lherzolite

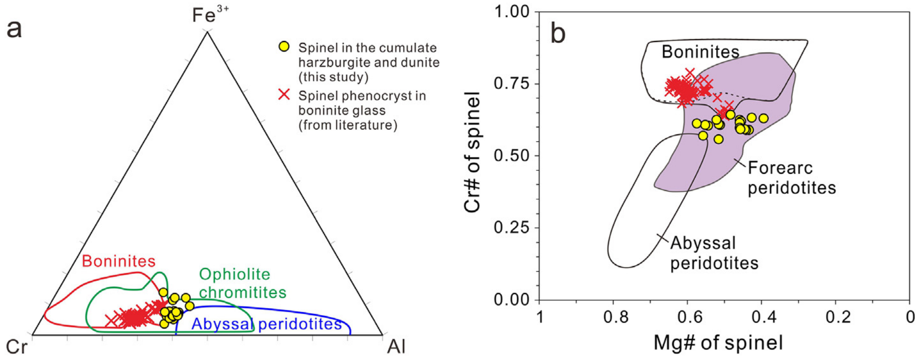

Fig. 8. Compositions of spinel in the cumulate harzburgite/lherzolite and dunite in this study (yellow circle) in the Trivalent Cr-Al-Fe^{3+} ternary cation diagram (a) and Cr# vs. Mg# diagram (b). Compositions of spinel in Troodos boninite glasses from the literature (Golowin et al., 2017; Woelki et al., 2018) are shown for comparison (red cross). The spinel compositional fields for boninites and ophiolite chromitites in (a) are from Barnes and Roeder (2001). Fields for boninites and forearc peridotite in (b) are modified from Tamura and Arai (2006) and Parkinson and Pearce (1998). Data of spinel compositions in abyssal peridotites are from Warren (2016). The dashed lines in (b) is the original boninite fields which is updated with solid lines based on the data in this study. The compositions of spinel in the cumulate harzburgite/lherzolite and dunite are close to those in boninite and lie in the field of ophiolite chromitites and forearc peridotites. (For interpretation of the references to colour in this figure legend, the reader is referred to the web version of this article.)

(Ol + Opx ± Cpx) cumulate must have formed as a straightforward consequence of boninite magma evolution. Indeed, the crystallization order of the ultramafic cumulate from the Pano Amiandos is reported as Ol → Opx → Cpx → Plg (Chum, 2014), which is different from that of the ultramafic cumulate commonly found in the Troodos ophiolite such as in the drill hole CY-4 (Ol → Cpx → Opx → Plg; George, 1978; Thy, 1987b; Browning et al., 1989). These observations and understanding thus point to the genetic link between the boninite (Fig. 2d–f) and the interlayered cumulate of dunite and harzburgite/lherzolite (Fig. 2a–c).

6.2. Major element compositional evidence for genetic link of boninite with the layered ultramafic cumulate

Spinels have been shown to be an effective tool to constrain parental melt compositions of cumulate rocks (e.g. Allahyari et al., 2014; Arai, 1994; Kamenetsky et al., 2001; Rollinson, 2008; Saccani and Tassinari, 2015). Experimental studies have shown direct relationship between compositions of melt and spinel in terms of Al_2O_3 and TiO_2 (Kamenetsky et al., 2001; Wasylenki et al., 2003). Rollinson (2008) has derived expressions using spinel compositions to calculate Al_2O_3 and TiO_2 contents in parental melts in arc-type settings:

$$Al_2O_3\ (\text{melt}) = 5.2181 \times \text{Ln}\ (Al_2O_3\ \text{in spinel}) – 1.0505$$

$$TiO_2\ (\text{melt}) = 1.0963 \times TiO_2\ (\text{spinel})^{0.7863}$$

Using this approach, we calculated Al_2O_3 and TiO_2 contents of the parental melt in equilibrium with spinels in the cumulate dunite and harzburgite/lherzolite (Fig. 9). Contents of Al_2O_3 and TiO_2 in boninite glasses from the literature (Woelki et al., 2018) and different tectonic settings are shown for comparison. The inferred melt has relatively lower Al_2O_3 (13.27–14.84 wt%) and TiO_2 (0.19–0.28 wt%) than MORB and island arc tholeiite (IAT). The Al_2O_3 and TiO_2 contents in boninite glasses (13.38–15.24 wt% and 0.25–0.38 wt%, respectively) are similar to those of the calculated melt parental to the cumulate dunite and harzburgite/lherzolite, in support of the hypothesis that the interlayered dunite and harzburgite/lherzolite cumulate of Troodos is most likely the product crystallized from a boninite parental magma.

6.3. Trace element compositional evidence for genetic link of boninite with the layered ultramafic cumulate

If the cumulate harzburgite/lherzolite (and dunite) is indeed the crystallization product of the evolving boninite melt, the minerals in harzburgite/lherzolite should be in equilibrium with the melt represented by boninite lavas in the Troodos ophiolite. By using mineral-melt partition coefficients, we calculated the incompatible trace element compositions of melts in equilibrium with average compositions of clinopyroxene (Mg# = 0.90) and orthopyroxene (Mg# = 0.89) in the cumulate harzburgite/lherzolite.

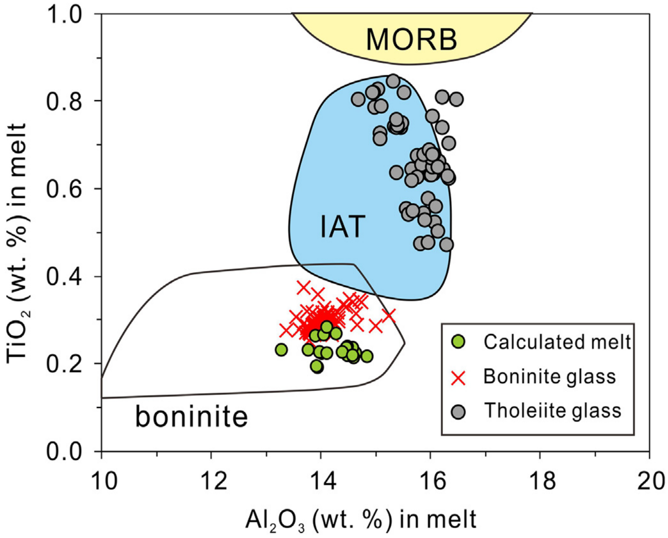

Fig. 9. Comparison of the calculated parental melt compositions (TiO_2 vs. Al_2O_3) in equilibrium with spinel of the studied ultramafic cumulate, boninite glass (Woelki et al., 2018) and tholeiite glasses in Troodos (Pearce and Robinson, 2010). The compositional fields of boninite, island arc tholeiitic (IAT) and MORB are drawn for comparison (modified from Allahyari et al. (2014) and Saccani and Tassinari (2015)). The calculated melts are characteristic of boninite in this well-studied major element compositional space.

Abundant pyroxene/melt partition coefficients (Kd's) are available in the literature for anhydrous basaltic systems (see Bédard, 1999, 2001; Klemme et al., 2002; Niu et al., 1996), but rare for hydrous basalt and boninite melts. Because the relevant incompatible element Kd's for wet hydrous systems are 2–3 times lower than in anhydrous melts (see McDade et al., 2003), we use the Kd data for dry basalts with half of the values in our calculation (Supplementary Table S8). Fig. 10 shows N-MORB normalized incompatible element patterns of such calculated melts in equilibrium with clinopyroxene and orthopyroxene in the cumulate harzburgite/lherzolite. The incompatible element patterns of calculated melts

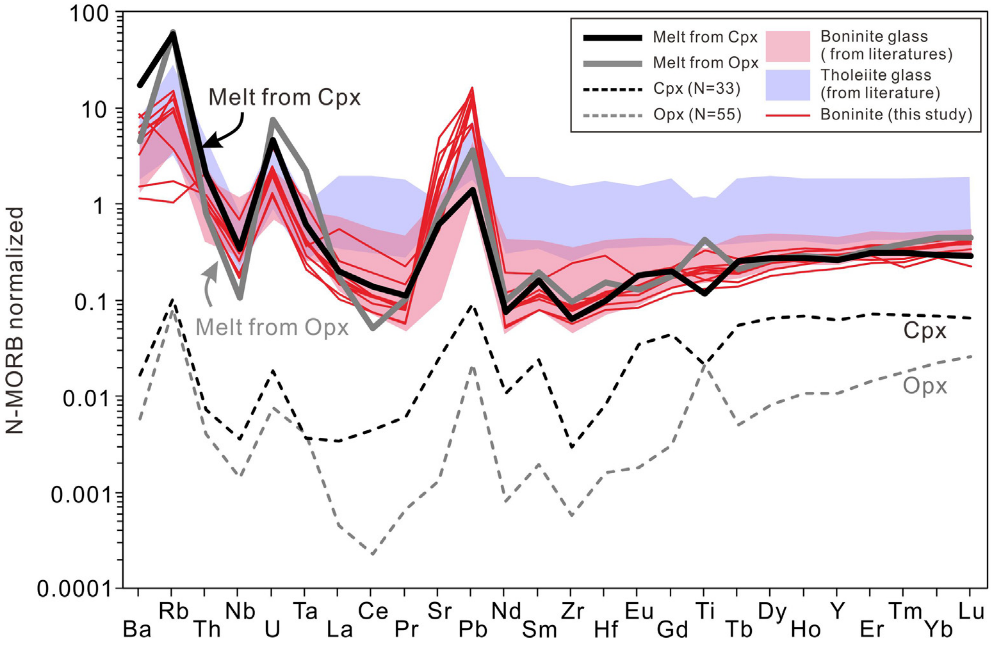

Fig. 10. N-MORB normalized incompatible element abundances of average clinopyroxene (Cpx) and orthopyroxene (Opx) in the cumulate harzburgite/lherzolite, calculated melts in equilibrium with the Cpx and Opx and boninite in this study. Fields for the boninite glass (Golowin et al., 2017; Woelki et al., 2018) and tholeiite glasses (Regelous et al., 2014) from the Troodos ophiolite are shown for comparison. The calculated melts in equilibrium with Cpx and Opx in the cumulate share the same trace element systematics as the Troodos boninite, pointing to their genetic link. Relative standard deviation (RSD) of REE for Cpx is within 20% except for La, Ce, Pr, Nd and Sm (within 30%). RSD of REE for Opx is higher (> 30% for La, Ce, Pr, Nd, Sm, Eu, Gd and Tb) due to the lower concentrations, but the effect of this fluctuation on the melt calculated from Opx is within the boninite glass field.

in equilibrium with both Cpx and Opx show remarkable similarity to those of the Troodos boninite lavas (Fig. 10). There is also significant correlation for all the incompatible element abundances between the calculated melts in equilibrium with Cpx and Opx ($R_{\text{Cpx-melt}} = 0.95$ and $R_{\text{Opx-melt}} = 0.93$) and the average Troodos boninite glass composition. Most incompatible elements of the calculated melts overlap well with those of boninite samples (boninite glasses from the literature and boninite samples in this study) (Fig. 10).

The remarkable similarity in incompatible element abundances and systematics we present here offer evidence that the orthopyroxene and clinopyroxene in the cumulate harzburgite/lherzolite are in equilibrium with melts represented by the boninite in the Troodos ophiolite. Some of the mantle harzburgites/dunites in Troodos have been shown to be equilibrated with the migrating melts (boninites or some depleted unknown melts) and are suggested to be formed by melt percolation or melt-rock reaction (Batanova and Sobolev, 2000; Büchl et al., 2002). However, the ultramafic rocks we study are not deformed massive mantle residual harzburgite with irregular dunite dikes and veins, but have typical cumulate textures (Figs. 3 & 4) and harzburgite/lherzolite-dunite interlayering (Fig. 2a–c). Moreover, in terms of mineral chemistry, the interlayered harzburgite/lherzolite-dunite rocks have lower Fo of olivine (87–89), lower Mg# and higher FeOt of Cpx (see Fig. 8) than the mantle dunite and harzburgite that have undergone melt percolation (Batanova and Sobolev, 2000; Büchl et al., 2002). Hence, the data and understanding support our hypothesis that the interlayered harzburgite/lherzolite-dunite rocks in Troodos are of cumulate origin resulting from boninite magma evolution.

6.4. Liquid lines of descent evidence for genetic link of boninite with the layered ultramafic cumulate

We use Petrolog 3.1.1.3 software (Danyushevsky and Plechov, 2011) to simulate the liquid lines of descent (LLDs) of the Troodos boninite. The primary magma compositions for the Troodos boninite lavas can be inferred by calculation or using olivine melt inclusions (Duncan and Green, 1980; Falloon and Danyushevsky, 2000; Golowin et al., 2017; Portnyagin et al., 1997). We choose a primary Troodos boninite magma composition used by Golowin et al. (2017) because it was calculated from a boninite glass sample near the AFZ (TRV-353, Supplementary Table S9). High water content in the primary boninite magma is estimated in the literature (e.g. Dobson et al., 1995; Falloon and Danyushevsky, 2000; Sobolev and Chaussidon, 1996; Thy, 1987a). We use a water content of 4 wt% in the modeling. The initial oxidation state of magma is set to be QMF + 1 (Pearce and Robinson, 2010). Olivine, plagioclase, clinopyroxene and orthopyroxene are chosen as possible liquidus phases.

The modeled compositions of the residual melts (Fig. 11) and the crystallized cumulate (dunite, harzburgite and lherzolite, Supplementary Table S10) are most consistent with the compositions of boninite glasses and the interlayered ultramafic cumulate under 0.1 GPa. The liquidus minerals appear in the order of olivine (at $MgO_{\text{melt}} = 14.8$ wt%), orthopyroxene (at $MgO_{\text{melt}} = 10.9$ wt%), clinopyroxene (at $MgO_{\text{melt}} = 8.9$ wt%) and plagioclase (very late, at $MgO_{\text{melt}} = 3.3$ wt%) (Fig. 11). In the modeling, dunite, harzburgite and lherzolite can be produced after 1–14%, 15–24% and 25–29% crystallization respectively (see Supplementary Table S10). The LLD paths of major elements of the melt overlap well with the data from the boninite glasses (Fig. 11). Meanwhile, the Mg# of the modeled melt after 12–23% crystallization (Mg# = 0.66–0.73) is very close to that of the boninite glass (Mg# = 0.65–0.72; Woelki et al., 2018), which shows similar degree of magma evolution. The modeling also indicates that fractional crystallization of boninite may occur at a shallow depth (~3 km) in a magma chamber. In summary, the modeling results match well with the compositions of both the ultramafic cumulate (i.e., rocks with the assemblage of the liquidus minerals: Ol → Ol + Opx → Ol + Opx + Cpx) and the boninite melt, which offer another line of evidence further in support of our hypothesis that the interlayered dunite (Ol) and harzburgite/lherzolite (Ol + Opx ± Cpx) cumulate in the Troodos ophiolite is the product of fractional crystallization of boninite magmas.

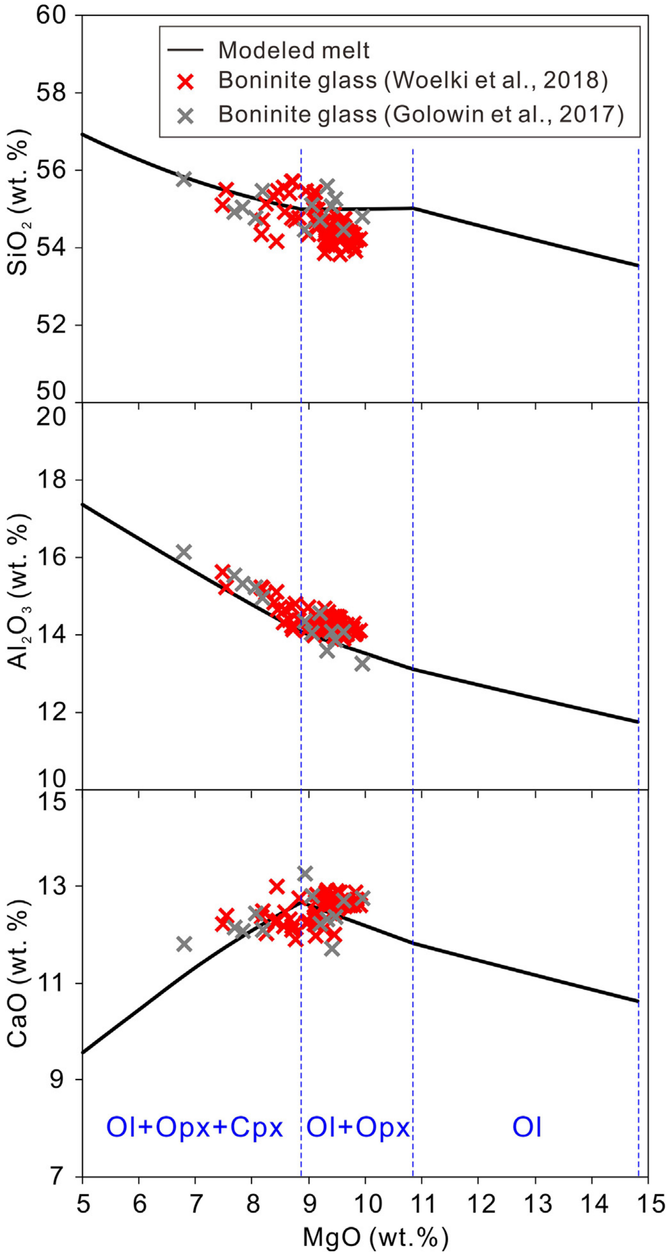

Fig. 11. The Troodos boninite glass compositions in SiO2, Al2O3 and CaO vs. MgO spaces (Golowin et al., 2017; Woelki et al., 2018) can be modeled to be consistent with liquid lines of descent using Petrolog 3.1.1.3 (Danyushevsky and Plechov, 2011). The start composition is the primary magma used by Golowin et al. (2017) from boninite in Troodos (Mg# = 0.78) (Supplementary Table S9). The liquidus phases crystallized can readily explain the layered ultramafic cumulate we study. Under 0.1 GPa with a crystallization order of Ol → Opx → Cpx, the cumulate dunite, harzburgite and lherzolite can be produced, respectively, after 1–14%, 15–24% and 25–29% fractional crystallization (see Supplementary Table S10). Thus, the observations and modeling all support the hypothesis that the cumulate dunite-harzburgite/lherzolite result from boninite magma evolution.

6.5. Development of the interlayered dunite and harzburgite/lherzolite during boninite magmatism

The foregoing demonstrations using petrography, mineral chemistry, and melt modeling offer strong lines of evidence in support of our hypothesis that the interlayered dunite-harzburgite/lherzolite rocks in the Troodos ophiolite complex (Fig. 2a-c) are of cumulate origin resulting from boninite magma evolution. We now show how the interlayered dunite and harzburgite (locally lherzolite) cumulate may have developed in terms of understood phase equilibria during boninite magma evolution.

As boninite has liquidus phases of Ol, Opx and minor Cpx, we can examine the phase relationships involving melt-Ol-Opx-Cpx to illustrate the development of the interlayered dunite and harzburgite/lherzolite cumulate. Experimental studies on multiple component natural systems are rare, but available experimental data on simple SiO$_2$-MgO-CaO system with melt-Fo-En-Di endmember phase equilibria can be used to approximate the natural melt-Ol-Opx-Cpx system to illustrate the concept and development of the inter-layered dunite-harzburgite cumulate. Because of the incongruent melting of enstatite at the pressure < 2 GPa (Presnall et al., 1978), very few experimental studies focusing directly on the Fo-En-Di system. However, we can construct a ternary Fo-En-Di phase diagram using existing experimental data (Boyd et al., 1964; Davis and England, 1964; Inoue, 1994; Kushiro, 1969; Presnall et al., 1978; Williams and Kennedy, 1969) to illustrate the concept as shown in Fig. 12. The temperature contours are for the Fo-En-Di system at 2 GPa would be significantly lower for multi-component natural systems especially for the hydrous boninitic systems, and the position of the eutectics may shift slightly under hydrous condition and lower pressure (Kushiro, 1969; van der Laan, 1987), but the concept we illustrate is valid and insightful as melt evolves and crystallization takes place during cooling.

Assuming point A (Fig. 12) represents the composition of the primary boninite magma, it begins to crystallize forsterite with cooling, leading to the melt move away from Fo towards the Fo-En cotectic while precipitating dunite cumulate in a magma chamber (A → B in Fig. 12). Continued cooling and crystallization of Fo with dunite cumulate formation, the melt eventually reaches the Fo-En cotectic and both Fo and En coprecipitate to form harzburgite cumulate overlaying the earlier dunite layer (C → D in Fig. 12). Periodic primary boninite melt replenishment into the magma chamber will result in the above process to repeat, thus leading to the interlayered dunite-harzburgite cumulate (Fig. 2a–c). The thickness of individual layers depends on both the frequency of melt supply pulses and the volume of each melt pulse. Importantly, delayed melt supply can lead to Fo-En coprecipitation along the cotectic line to reach the Fo-En-Di eutectic (E in Fig. 12), leading to the coprecipitation of clinopyroxene and the formation of harzburgite with minor Cpx or localized lherzolite, which is consistent with our observations (see above).

The formation of interlayered dunite-harzburgite/lherzolite cumulate in the Troodos ophiolite complex can be briefly summarized as crystallization of boninite magma and periodic magma injections into an open magma chamber as illustrated in Fig. 12, in cycles of a → b → c → (d) → a → b → c → (d)…

Magmatic layering could be caused by several processes such as convection-related processes (Naslund et al., 1991) and deformation of crystal mush (Jousselin et al., 2012). These could be other processes taking place in the magma chamber, but all these speculations are hard to test. Besides, mechanical processes such as gravitational sorting are unlikely because our observed layers are generally quite thin and as thin as millimeters without grainsize grading. Our hypothesis is the simplest and is physically most plausible process that agrees with the petrologic and geochemical characteristics.

Corresponding to the phase equilibrium analysis (Fig. 12), Fig. 13 illustrates the evolution of boninite magma and the petrogenesis of the interlayered dunite-harzburgite/lherzolite cumulate. Boninite melt originates from high degree partial melting of refractory harzburgitic mantle sources as the result of water introduction at high temperatures (Falloon and Danyushevsky, 2000; Kostopoulos and Murton, 1992; Li et al., 2013). Crystallization of boninite melt in an open magma chamber leads to the formation of the interlayered dunite-harzburgite/lherzolite cumulate (Fig. 13a). The parental melt begins to crystallize olivine to form a dunite layer (A → C in Fig. 12), and the continued crystallization along the Fo-En cotectic and Fo-En-Di eutectic will produce harzburgite/lherzolite layer (C → D → E in Fig. 12) (Fig. 13b). Primitive melt with

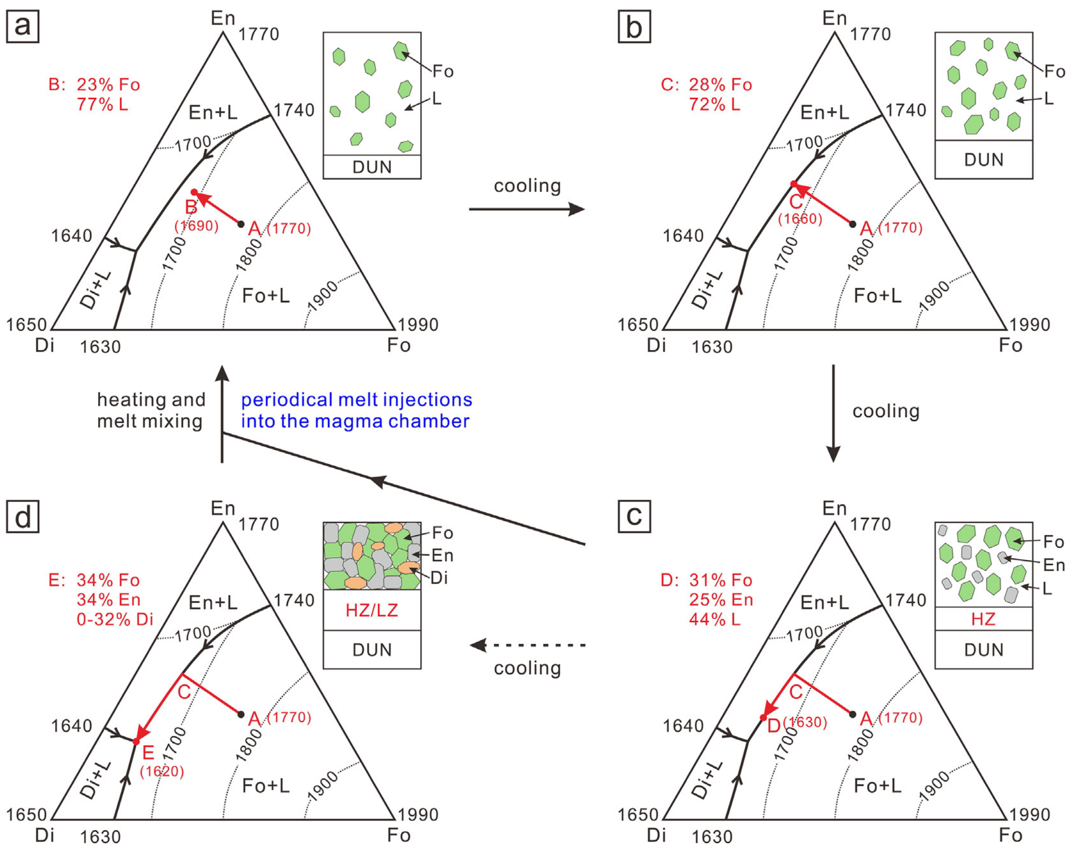

Fig. 12. Simplified Forsterite (Fo)-Enstatite (En)-Diopside (Di) ternary phase diagrams to approximate the natural Ol-Opx-Cpx phase relationships to illustrate the petrogenesis of the interlayered dunite and harzburgite/lherzolite cumulate in the Troodos ophiolite. The dashed lines are isotherms at intervals of 100 °C and the solid lines are cotectic lines. The melting temperatures for Fo, En, Di are from Davis and England (1964), Boyd et al. (1964), Williams and Kennedy (1969). The eutectic temperatures of Di-En, Fo-Di and Fo-En joins at 2 GPa are from Kushiro (1969), Presnall et al. (1978) and Inoue (1994) respectively. Note that the natural water saturated Ol-Opx-Cpx systems appropriate for boninite magmatism necessarily have lower temperatures than these dry Fo-En-Di systems, but the concept and process we show are valid demonstrations. The parental melt begins to crystallize olivine to form a dunite layer before reaching the Ol-Opx cotectic (A → B), along which Ol and Opx coprecipitate to form a harzburgite layer (C → D). The melt will evolve to the Ol-Opx-Cpx eutectic (E) to form harzburgite with some Cpx or lherzolite if the replenishment is delayed. Periodical melt injection into the magma chamber results in dunite-harzburgite interlayered cumulate, in cycles of a → b → c → (d) → a → b → c → (d)…. L, liquid; DUN, dunite; HZ, harzburgite; LZ, lherzolite.

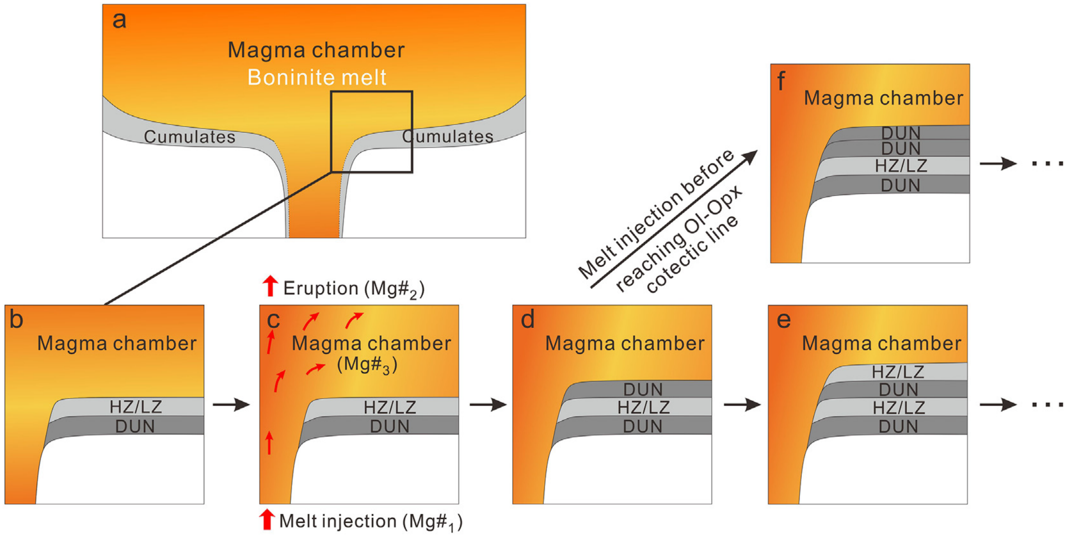

Fig. 13. Schematic illustration showing the formation of the interlayered dunite (DUN) and harzburgite (HZ)/lherzolite (LZ) cumulate. The cumulate sequence is best understood as the result of fractional crystallization of periodically replenished mantle-derived boninite melts as illustrated in terms of phase equilibria (Fig. 12) and schematically in (a). (b-f) illustrate the development of the cumulate. After the formation of a dunite-harzburgite/lherzolite sequence in a magma chamber (b, Fig. 11), primitive melt ($Mg\#_1$) with high temperature injects into the magma chamber (c). The erupted melt ($Mg\#_2$) consists of much of the newly replenished primitive melt having $Mg\#_1$ mixed with the existing prior evolved melt. The unerupted melt mixing with the evolved melt in the magma chamber ($Mg\#_3$) continue the crystallization to form next cumulate layers (c–e, f). That is, the interlayered cumulate forms as resulting from periodically replenished (injected) and periodically erupted steady-state open magma chamber system. The varying thickness of the layers (see Fig. 2a–c) reflects varying frequency and varying volume of melt supply pulses.

high temperature and high Mg# ($Mg\#_1$) injects into the magma chamber, which, mixed with some existing melt, will soon erupt under increased pressure ($Mg\#_2$). The unerupted melt can mix more thoroughly with the evolved melts in the magma chamber to continue the crystallization as above ($Mg\#_3$), forming layered dunite-harzburgite/lherzolite cumulate (Fig. 13c–e, f). It is important to note that this repeated cycling process will lead to melt compositional changes with $Mg\#_1 > Mg\#_2 > Mg\#_3$ (Fig. 13c). Hence, olivine phenocrysts from boninite glasses have higher Fo than olivine in the cumulate (Fig. 6).

7. Conclusions

In this paper, we report the interlayered dunite-harzburgite/lherzolite rock association in the Troodos ophiolite complex. We hypothesize that this rock association is of magmatic cumulate origin as the result of boninite magma evolution. We have successfully tested and proved this hypothesis by using field and petrographic observations, mineral chemistry, major and trace element compositions, petrological modeling, and phase equilibrium analysis.

(1) This understanding represents an important novel petrological contribution.

(2) With Ol and Opx being the liquidus phases and with the interlayered dunite (Ol)-harzburgite/lherzolite (Ol + Opx ± Cpx) rock association, we hypothesize that the latter is of cumulate origin as a result of straightforward consequence of boninite magma evolution.

(3) The melts in equilibrium with spinels in the cumulate harzburgite/lherzolite and dunite are characteristically boninitic in terms of major element compositions (e.g., TiO_2 and Al_2O_3).

(4) The calculated melts in equilibrium with Cpx and Opx in the cumulate harzburgite/lherzolite share the same trace element patterns as the Troodos boninite (both glasses and bulk-rock compositions).

(5) Petrological modeling of the boninite melt evolution shows a crystallization order of Ol → Opx → Cpx → Plg, indicating that the cumulate dunite and harzburgite (locally lherzolite) in the Troodos ophiolite can be produced by fractional crystallization of the primary boninite melt at 0.1 GPa.

(6) The petrogenesis of the interlayered dunite-harzburgite/lherzolite cumulate is best understood as the result of fractional crystallization of periodically replenished and periodically erupted open magma chamber with the primitive boninite melt derived from depleted mantle sources.

(7) We emphasize it important to consider dunite-harzburgite/lherzolite cumulate when interpreting seismic structure of the crust in subduction settings, especially in rock sequences associated with subduction initiation thought to be indicated by boninite magmatism.

Declaration of Competing Interest

The authors declare that they have no known competing financial interests or personal relationships that could have appeared to influence the work reported in this paper.

Acknowledgements

We thank the company of Iain Neill, Peter Tollan and Durham 3rd year students during our annual Troodos field trips. We thank Akihiro Tamura and anonymous reviewers for constructive reviews, and Michael Roden for editorial handling. This study is supported by the National Natural Science Foundation of China (41630968), the NSFC-Shandong Joint Fund for Marine Science Research Centers (U1606401), the National Natural Science Foundation of China (91958215), Qingdao National Laboratory for Marine Science and Technology (2015ASKJ03), and the 111 Project (B18048).

Appendix A. Supplementary data

Supplementary data to this article can be found online at https://doi.org/10.1016/j.lithos.2020.105764.

References

Allahyari, K., Saccani, E., Rahimzadeh, B., Zeda, O., 2014. Mineral chemistry and petrology of highly magnesian ultramafic cumulates from the Sarve-Abad (Sawlava) ophiolites (Kurdistan, NW Iran): New evidence for boninitic magmatism in intra-oceanic fore-arc setting in the Neo-Tethys between Arabia and Iran. J. Asian Earth Sci. 79, 312–328.

Arai, S., 1994. Characterization of spinel peridotites by olivine-spinel compositional relationships: review and interpretation. Chem. Geol. 113, 191–204.

Barnes, S.J., Roeder, P.L., 2001. The range of spinel compositions in terrestrial mafic and ultramafic rocks. J. Petrol. 42, 2279–2302.

Batanova, V.G., Sobolev, A.V., 2000. Compositional heterogeneity in subduction-related mantle peridotites, Troodos massif, Cyprus. Geology 28, 55–58.

Batanova, V.G., Sobolev, A.V., Schmincke, H.U., 1996. Parental melts of the intrusive cumulates of the Troodos massif, Cyprus: a study of clinopyroxenes and melt inclusions in plagioclase. Petrology 4, 255–264.

Bédard, J.H., 1999. Petrogenesis of boninites from the Betts Cove ophiolite, Newfoundland, Canada: identification of subducted source components. J. Petrol. 40, 1853–1889.

Bédard, J.H., 2001. Parental magmas of the Nain Plutonic Suite anorthosites and mafic cumulates: a trace element modelling approach. Contrib. Mineral. Petrol. 141, 747–771.

Bednarz, U., Schmincke, H., 1994. Petrological and chemical evolution of the northeastern Troodos Extrusive Series, Cyprus. J. Petrol. 35, 489–523.

Benn, K., Laurent, R., 1987. Intrusive suite documented in the Troodos ophiolite plutonic complex, Cyprus. Geology 15, 821–824.

Boyd, F., England, J., Davis, B.T., 1964. Effects of pressure on the melting and polymorphism of enstatite, $MgSiO_3$. J. Geophys. Res. 69, 2101–2109.

Browning, P., Roberts, S., Alabaster, T., 1989. Fine scale modal layering and cyclic units in ultramafic cumulates from the CY-4 borehole, Troodos ophiolite: evidence for an open system magma chamber. Cyprus Crustal Study Project: Initial Report, Hole CY-4, Geological Survey of Canada, pp. 193–220.

Büchl, A., Brügmann, G., Batanova, V.G., Münker, C., Hofmann, A.W., 2002. Melt percolation monitored by Os isotopes and HSE abundances: a case study from the mantle section of the Troodos Ophiolite. Earth Planet. Sci. Lett. 204, 385–402.

Cameron, W.E., 1985. Petrology and origin of primitive lavas from the Troodos ophiolite, Cyprus. Contrib. Mineral. Petrol. 89, 239–255.

Cameron, W.E., Nisbet, E.G., Dietrich, V.J., 1979. Boninites, komatiites and ophiolitic basalts. Nature 280, 550.

Cameron, W.E., McCulloch, M.T., Walker, D.A., 1983. Boninite petrogenesis: chemical and Nd-Sr isotopic constraints. Earth Planet. Sci. Lett. 65, 75–89.

Cawthorn, R.G. (Ed.), 1996. Layered Intrusions. Elsevier, New York, p. 531.

Charlier, B., Namur, O., Latypov, R., Tegner, C. (Eds.), 2015. Layered Intrusions. Springer, London, p. 748.

Chen, S., Wang, X., Niu, Y., Sun, P., Duan, M., Xiao, Y., Guo, P., Gong, H., Wang, G., Xue, Q., 2017. Simple and cost-effective methods for precise analysis of trace element abundances in geological materials with ICP-MS. Sci. Bull. 62, 277–289.

Chen, Y., Niu, Y., Shen, F., Gao, Y., Wang, X., 2020. New U-Pb zircon age and petrogenesis of the plagiogranite, Troodos ophiolite. Cyprus. Lithos https://doi.org/10.1016/j.lithos.2020.105472.

Chum, C., 2014. Cumulate Pyroxenite and Pyroxenite Dykes in the Troodos Ophiolite, Cyprus. Master dissertation. The University of Hongkong.

Coleman, R.G., Keith, T.E., 1971. A chemical study of serpentinization—Burro Mountain, California. J. Petrol. 12, 311–328.

Coogan, L., Banks, G., Gillis, K., MacLeod, C., Pearce, J., 2003. Hidden melting signatures recorded in the Troodos ophiolite plutonic suite: evidence for widespread generation of depleted melts and intra-crustal melt aggregation. Contrib. Mineral. Petrol. 144, 484–506.

Crawford, A.J., Falloon, T.J., Green, D.H., 1989. Classification, Petrogenesis and Tectonic Setting of Boninites.

Danyushevsky, L.V., Plechov, P., 2011. Petrolog3: Integrated software for modeling crystallization processes. Geochem. Geophys. Geosyst. 12. https://doi.org/10.1029/2011GC003516.

Davis, B., England, J., 1964. The melting of forsterite up to 50 kilobars. J. Geophys. Res. 69, 1113–1116.

Dick, H.J.B., Fisher, R.L., Bryan, W.B., 1984. Mineralogical variability of the uppermost mantle along mid-ocean ridges. Earth Planet. Sci. Lett. 69, 88–106.

Dobson, P.F., Skogby, H., Rossman, G.R., 1995. Water in boninite glass and coexisting orthopyroxene: concentration and partitioning. Contrib. Mineral. Petrol. 118, 414–419.

Droop, G.T.R, 1987. A general equation for estimating Fe^{3+} concentrations in ferromagnesian silicates and oxides from microprobe analyses, using stoichiometric criteria. Mineralogical Magazine 51, 431–435.

Duncan, R.A., Green, D., 1980. Role of multistage melting in the formation of oceanic crust. Geology 8, 22–26.

Duncan, R.A., Green, D.H., 1987. The genesis of refractory melts in the formation of oceanic crust. Contrib. Mineral. Petrol. 96, 326–342.

Falloon, T.J., Danyushevsky, L.V., 2000. Melting of refractory mantle at 1.5, 2 and 2.5 GPa under anhydrous and H_2O-undersaturated conditions: Implications for the petrogenesis of high-Ca boninites and the influence of subduction components on mantle melting. J. Petrol. 41, 257–283.

Flower, M.F.J., Levine, H.M., 1987. Petrogenesis of a tholeiite-boninite sequence from Ayios Mamas, Troodos ophiolite: evidence for splitting of a volcanic arc? Contrib. Mineral. Petrol. 97, 509–524.

George, R.P., 1978. Structural petrology of the Olympus ultramafic complex in the Troodos ophiolite, Cyprus. Geol. Soc. Am. Bull. 89, 845–865.

Golowin, R., Portnyagin, M., Hoernle, K., Sobolev, A., Kuzmin, D., Werner, R., 2017. The role and conditions of second-stage mantle melting in the generation of low-Ti tholeiites and boninites: the case of the Manihiki Plateau and the Troodos ophiolite. Contrib. Mineral. Petrol. 172, 104.

Greenbaum, D., 1972. Magmatic processes at ocean ridges: evidence from the Troodos massif, Cyprus. Nat. Phys. Sci. 238, 18–21.

Inoue, T., 1994. Effect of water on melting phase relations and melt composition in the system Mg_2SiO_4-$MgSiO_3$-H_2O up to 15 GPa. Phys. Earth Planet. Inter. 85, 237–263.

Irvine, T.N., Smith, C.H., 1967. The Ultramafic Rocks of the Muskox Intrusion, Northwest Territories, Canada. Ultramafic and Related Rocks, Wiley, New York, pp. 38–49.

Jaques, A.L., Green, D.H., 1980. Anhydrous melting of peridotite at 0–15 kb pressure and the genesis of tholeiitic basalts. Contrib. Mineral. Petrol. 73, 287–310.

Jousselin, D., Morales, L.F., Nicolle, M., Stephant, A., 2012. Gabbro layering induced by simple shear in the Oman ophiolite Moho transition zone. Earth Planet. Sci. Lett. 331, 55–66.

Kamenetsky, V.S., Crawford, A.J., Meffre, S., 2001. Factors controlling chemistry of magmatic spinel: an empirical study of associated olivine, Cr-spinel and melt inclusions from primitive rocks. J. Petrol. 42, 655–671.

Klemme, S., Blundy, J.D., Wood, B.J., 2002. Experimental constraints on major and trace element partitioning during partial melting of eclogite. Geochim. Cosmochim. Acta 66, 3109–3123.

Kong, J., Niu, Y., Sun, P., Xiao, Y., Guo, P., Hong, D., Zhang, Y., Shao, F., Wang, X., Duan, M., 2019. The origin and geodynamic significance of the Mesozoic dykes in eastern continental China. Lithos. 332, 328–339.

König, S., Münker, C., Schuth, S., Garbe-Schönberg, D., 2008. Mobility of tungsten in subduction zones. Earth Planet. Sci. Lett. 274, 82–92.

Konstantinou, A., Wirth, K., Vervoort, J., 2007. U-Pb isotopic dating of Troodos plagiogranite, Cyprus by LA-ICP-MS. Geol. Soc. Am. Abstr. Programs 39, 388.

Kostopoulos, D., Murton, B., 1992. Origin and distribution of components in boninite genesis: significance of the OIB component. Geol. Soc. Lond. Spec. Publ. 60, 133–154.

Kushiro, I., 1969. The system forsterite-diopside-silica with and without water at high pressures. Am. J. Sci. 267, 269–294.

Laurent, R., 1992. Peridotite intrusions emplaced in the fossil suprasubduction zone environment of Cyprus. Geol. Soc. Lond. Spec. Publ. 60, 233–239.

Le Bas, M.J., 2000. IUGS reclassification of the high-Mg and picritic volcanic rocks. J. Petrol. 41, 1467–1470.

Li, Y., Kimura, J.I., Machida, S., Ishii, T., Ishiwatari, A., Maruyama, S., Qiu, H., Ishikawa, T., Kato, Y., Haraguchi, S., Takahata, N., Hirahara, Y., Miyazaki, T., 2013. High-Mg Adakite and Low-Ca Boninite from a Bonin Fore-arc Seamount: Implications for the Reaction between Slab Melts and Depleted Mantle. J. Petrol. 54, 1149–1175.

Liu, Y., Hu, Z., Gao, S., Günther, D., Xu, J., Gao, C., Chen, H., 2008. In situ analysis of major and trace elements of anhydrous minerals by LA-ICP-MS without applying an internal standard. Chem. Geol. 257, 34–43.

McDade, P., Blundy, J.D., Wood, B.J., 2003. Trace element partitioning between mantle wedge peridotite and hydrous MgO-rich melt. Am. Mineral. 88, 1825–1831.

Moores, E.M., Vine, F.J., 1971. The Troodos Massif, Cyprus and other ophiolites as oceanic crust: evaluation and implications. Philosophical transactions of the Royal Society of London. Series A. Math. Phys. Sci. 268, 443–467.

Mukasa, S.B., Ludden, J.N., 1987. Uranium-lead isotopic ages of plagiogranites from the Troodos ophiolite, Cyprus, and their tectonic significance. Geology 15, 825–828.

Naslund, H.R., Turner, P.A., Keith, D.W., 1991. Crystallization and layer formation in the middle zone of the Skaergaard Intrusion. Bull. Geol. Soc. Den. 38, 165–171.

Niu, Y., 1997. Mantle melting and melt extraction processes beneath ocean ridges: evidence from abyssal peridotites. J. Petrol. 38, 1047–1074.

Niu, Y., 2004. Bulk-rock major and trace element compositions of abyssal peridotites: implications for mantle melting, melt extraction and post-melting processes beneath mid-ocean ridges. J. Petrol. 45, 2423–2458.

Niu, Y., Waggoner, D.G., Sinton, J.M., Mahoney, J.J., 1996. Mantle source heterogeneity and melting processes beneath seafloor spreading centers: the East Pacific rise, 18–19°S. J. Geophys. Res. Solid Earth 101, 27711–27733.

Niu, Y., Langmuir, C.H., Kinzler, R.J., 1997. The origin of abyssal peridotites: a new perspective. Earth Planet. Sci. Lett. 152, 251–265.

O'Hanley, D.S., 1992. Solution to the volume problem in serpentinization. Geology 20, 705–708.

Osozawa, S., Shinjo, R., Lo, C.H., Jahn, B.M., Hoang, N., Sasaki, M., Ishikawa, K.I., Kano, H., Hoshi, H., Xenophontos, C., Wakabayashi, J., 2012. Geochemistry and geochronology of the Troodos ophiolite: an SSZ ophiolite generated by subduction initiation and an extended episode of ridge subduction? Lithosphere 4, 497–510.

Parkinson, I.J., Pearce, J.A., 1998. Peridotites from the Izu–Bonin–Mariana forearc (ODP Leg 125): evidence for mantle melting and melt–mantle interaction in a supra-subduction zone setting. J. Petrol. 39, 1577–1618.

Pearce, J.A., Robinson, P.T., 2010. The Troodos ophiolitic complex probably formed in a subduction initiation, slab edge setting. Gondwana Res. 18, 60–81.

Portnyagin, M., Danyushevsky, L., Kamenetsky, V., 1997. Coexistence of two distinct mantle sources during formation of ophiolites: a case study of primitive pillow-lavas from the lowest part of the volcanic section of the Troodos Ophiolite, Cyprus. Contrib. Mineral. Petrol. 128, 287–301.

Presnall, D., Dixon, S.A., Dixon, J.R., O'donnell, T., Brenner, N., Schrock, R., Dycus, D., 1978. Liquidus phase relations on the join diopside-forsterite-anorthite from 1 atm to 20 kbar: their bearing on the generation and crystallization of basaltic magma. Contrib. Mineral. Petrol. 66, 203–220.

Raedeke, L.D., McCallum, I.S., 1984. Investigations in the Stillwater complex: Part II. Petrology and petrogenesis of the ultramafic series. J. Petrol. 25, 395–420.

Regelous, M., Haase, K.M., Freund, S., Keith, M., Weinzierl, C.G., Beier, C., Brandl, P.A., Endres, T., Schmidt, H., 2014. Formation of the Troodos Ophiolite at a triple junction: evidence from trace elements in volcanic glass. Chem. Geol. 386, 66–79.

Resing, J.A., Rubin, K.H., Embley, R.W., Lupton, J.E., Baker, E.T., Dziak, R.P., Baumberger, T., Lilley, M.D., Huber, J.A., Shank, T.M., Butterfield, D.A., Clague, D.A., Keller, N.S., Merle, S.G., Buck, N.J., Michael, P.J., Soule, A., Caress, D.W., Walker, S.L., Davis, R., Cowen, J.P., Reysenbach, A.L., Thomas, H., 2011. Active submarine eruption of boninite in the northeastern Lau Basin. Nat. Geosci. 4, 799–806.

Robinson, P.T., Melson, W.G., O'Hearn, T., Schmincke, H.U., 1983. Volcanic glass compositions of the Troodos ophiolite, Cyprus. Geology 11, 400–404.

Rollinson, H., 2008. The geochemistry of mantle chromitites from the northern part of the Oman ophiolite: inferred parental melt compositions. Contrib. Mineral. Petrol. 156, 273–288.

Saccani, E., Tassinari, R., 2015. The role of MORB and SSZ magma-types in the formation of Jurassic ultramafic cumulates in the Mirdita ophiolites (Albania) as deduced from chromian spinel and olivine chemistry. Ofioliti 40, 37–56.

Smewing, J.D., Simonian, K.O., Gass, I.G., 1975. Metabasalts from the Troodos Massif, Cyprus: genetic implication deduced from petrography and trace element geochemistry. Contrib. Mineral. Petrol. 51, 49–64.

Sobolev, A.V., Chaussidon, M., 1996. H_2O concentrations in primary melts from supra-subduction zones and mid-ocean ridges: implications for H_2O storage and recycling in the mantle. Earth Planet. Sci. Lett. 137, 45–55.

Stevens, R.E., 1944. Composition of some chromites of the western hemisphere. Am. Mineral. J. Earth Planet. Mater. 29, 1–34.

Sun, S.S., McDonough, W.F., 1989. Chemical and isotopic systematics of oceanic basalts: implications for mantle composition and processes. Geol. Soc. Lond. Spec. Publ. 42, 313–345.

Tamura, A., Arai, S., 2006. Harzburgite–dunite–orthopyroxenite suite as a record of supra-subduction zone setting for the Oman ophiolite mantle. Lithos 90, 43–56.

Taylor, R.N., Nesbitt, R.W., Vidal, P., Harmon, R.S., Auvray, B., Croudace, I.W., 1994. Mineralogy, chemistry, and genesis of the boninite series volcanics, Chichijima, Bonin Islands, Japan. J. Petrol. 35, 577–617.

Thy, P., 1987a. Petrogenetic implications of mineral crystallization trends of Troodos cumulates, Cyprus. Geol. Mag. 124, 1–11.

Thy, P., 1987b. Magmas and magma chamber evolution, Troodos ophiolite, Cyprus. Geology 15, 316.

Thy, P., Xenophontos, C., 1991. Crystallization orders and phase chemistry of glassy lavas from the pillow sequences, Troodos ophiolite, Cyprus. J. Petrol. 32, 403–428.

van der Laan, S.R., 1987. An experimental study of boninite genesis. Doctor dissertation. The University of Illinois at Chicago.

Warren, J.M., 2016. Global variations in abyssal peridotite compositions. Lithos 248, 193–219.

Wasylenki, L.E., Baker, M.B., Kent, A.J., Stolper, E.M., 2003. Near-solidus melting of the shallow upper mantle: partial melting experiments on depleted peridotite. J. Petrol. 44, 1163–1191.

Williams, D.W., Kennedy, G.C., 1969. Melting curve of diopside to 50 kilobars. J. Geophys. Res. 74, 4359–4366.

Woelki, D., Regelous, M., Haase, K.M., Romer, R.H.W., Beier, C., 2018. Petrogenesis of boninitic lavas from the Troodos Ophiolite, and comparison with Izu–Bonin–Mariana fore-arc crust. Earth Planet. Sci. Lett. 498, 203–214.

Xiao, Y., Chen, S., Niu, Y., Wang, X., Xue, Q., Wang, G., Gao, Y., Gong, H., Kong, J., Shao, F., Sun, P., Duan, M., Hong, D., Wang, D., 2020. Mineral compositions of syn-collisional granitoids and their implications for the formation of juvenile continental crust and adakitic magmatism. J. Petrol. https://doi.org/10.1093/petrology/egaa038 egaa038.